ELSEVIER

Remote Sensing of Environment 83 (2002) 112–134

Remote Sensing of Environment

www.elsevier.com/locate/rse

Land surface reflectance, emissivity and temperature from MODIS middle and thermal infrared data

François Petitcolin *, Eric Vermote[1]

Department of Geography, University of Maryland, College Park, MD 20942, USA
NASA's Goddard Space Flight Center, Code 923, Greenbelt, MD 20771, USA

Received 10 April 2001; received in revised form 24 February 2002; accepted 12 March 2002

Abstract

The following paper presents a method to retrieve surface reflectance, emissivity and temperature in the middle infrared (3–5 μm) and thermal infrared (8–12 μm). It is applied to Moderate Resolution Imaging Spectroradiometer (MODIS) data acquired over Southern Africa during the August to October 2000 period. This method relies first on atmospheric correction of the middle-thermal infrared radiances which uses National Center for Environmental Prediction (NCEP) humidity, pressure and temperature profiles and second on constructing and using a database of night emissivities ratio (Temperature Independent Spectral Indices of Emissivity, TISIE). The middle infrared reflectances (3–5 μm) are then derived from day-time measurements and mean TISIE values. By hemispheric integration (over a 16-day period), they lead to middle infrared directional emissivity which, combined with TISIE again, leads to thermal infrared emissivity and surface temperature. The reflectance accuracies are assessed by looking at targets of known reflectance (water and sun-glint). The emissivities in the thermal infrared are assessed by checking the spectral invariance of the derived surface temperature in the 3–5- and 8–12-μm region. Other consistency checks are performed leading to the conclusion that the reflectance, emissivity and surface temperature are derived within ± 0.015, ± 0.01 and ± 1 K, respectively. Finally, a direct application of the MODIS middle infrared surface reflectances to the fire detection problem is developed and the results compared to the Landsat 7 high spatial resolution data.

1. Introduction

With 15 emissive bands, the Moderate Resolution Imaging Spectroradiometer (MODIS) on-board the EOS-TERRA platform offers new perspectives in Earth observation in the infrared spectrum (3–15 μm). Because chemical components of the atmosphere have various absorption bands, only seven MODIS emissive bands are useful for land surface remote sensing (see Table 1). MODIS has four bands (20, 21, 22, 23) in the 3–5 μm atmospheric window. In this spectral region, called middle infrared, thermal emission and solar reflection of natural surfaces are in the same order of magnitude for day-time observations. With low gain, band 21, called the fire band, is designed to perform radiometric measurements over a very hot target without saturation. The 8–12 μm atmospheric window, with relatively low absorption from water vapor, is broken into two parts by the ozone absorption band around 9.75 μm. MODIS band 29 occupies the 8–9-μm window, and bands 31 and 32 the 10–12-μm window. These two bands are at the maximum of emission for targets at ambient temperature.

Surface properties in the infrared are specified either in terms of emissivity or reflectance, the emissivity being related to the directional hemispheric reflectance by Kirchhoff's law. The retrieval of emissivity in the infrared requires solving the emissivity/temperature separation problem.

In thermal infrared remote sensing, the number of unknowns (one spectral emissivity per band and the temperature) is always greater than the number of equations (one per band). Therefore, outcomes are limited to relative emissivity and land surface temperature with still uncertainties attached to it. Methods to extract relative emissivities have been compared by Li, Becker, Stoll, and Wan (1999).

* Corresponding author. Fax: +1-301-614-6695.
E-mail addresses: francois@kratmos.gsfc.nasa.gov (F. Petitcolin), eric@kratmos.gsfc.nasa.gov (E. Vermote).
[1] Fax: +1-301-614-6695.

0034-4257/02/$ - see front matter © 2002 Elsevier Science Inc. All rights reserved.
PII: S0034-4257(02)00094-9

Table 1
Summary of MODIS emissive bands dedicated to land applications

Band	Band width (μm)	Central wavelength (μm)	Required $Ne\Delta T$ (K)
20	3.660–3.8408	3.7882	0.05
21	3.929–3.989	3.9921	2.00
22	3.929–3.989	3.9719	0.07
23	4.020–4.080	4.0567	0.07
29	8.400–8.700	8.5288	0.05
31	10.78–11.28	11.0186	0.05
32	11.77–12.27	12.0325	0.05

As for the sea surface temperature (SST), the land surface temperature (LST) can be derived using the split-window technique and many algorithms have been published for various instruments ((see Quin & Karnieli, 1999) for a review), but the accuracy of the results is limited by the knowledge of the spectral emissivity and its angular variations. In the middle infrared, the surface reflectance can be derived by correcting for the thermal emission of the surface (Goïta & Royer, 1997; Nerry, Petitcolin, & Stoll, 1998; Roger & Vermote, 1998). Using Kirchhoff's law, the middle infrared emissivity is then computed, and the spectral signature in the infrared bands is achieved by means of relative emissivities. The middle infrared surface reflectance is a key to solving the emissivity/temperature separation problem.

Several methods to compute the middle infrared surface reflectance have been published. They all use surface brightness temperature in the thermal infrared to estimate the middle infrared surface emission during day-time observation. Assumptions on thermal infrared emissivities coming from various sources such as an empirical relation with NDVI (Roger & Vermote, 1998), theoretical simulations using a reference emissivity database (Goïta & Royer, 1997) (TSRAM model) have been used. Nerry et al.'s (1998) method is based on the Temperature Independent Spectral Indices of Emissivity (TISIE) concept (Becker & Li, 1990). This last method was selected for this work on MODIS data because it only assumes that the TISIE, which are ratios of surface emissivity raised to specific powers, are equal for consecutive day and night-time observations.

Two different approaches were adopted for the distributed MODIS land surface temperature and emissivity products. LST is derived using either a split-window method that takes into account the land surface emissivity (Snyder, Wan, Zhang, & Feng, 1998) or an original method that performs also atmospheric corrections and produces land surface emissivity, atmospheric water vapor content and equivalent air temperature as well (Wan & Li, 1997). In the presented method, atmospheric corrections are performed aside from the emissivity/temperature separation scheme and carefully checked.

MODIS data were acquired during the August 20th to October 24th, 2000 period over Southern Africa (from 10° to 35° South and from 10° to 40° East). During this period, MODIS was on A Side electronic and some MODIS bands have non-functional detector and stripes appear in these bands. Non-functional detectors have been identified and measurements from them have been discarded without any major consequence to our results. On November 1st, 2000, the instrument switched to B Side electronic and most of the non-functional detectors are now operating normally and better calibration is expected.

The first part of this paper is dedicated to the retrieval of middle infrared surface reflectance and spectral emissivity. As this method is not new but has been adapted to MODIS capabilities, we balanced our presentation of the method between definition of the quantities, their physical relations and operational data processing approach. This first part includes five sections focusing on atmospheric corrections, emissivity ratios, middle infrared reflectance, directional emissivity and land surface temperature.

The second part is devoted to the comparison or validation of our results with independent measurements or outputs of the model. For example, we compared land surface temperature retrieved using different MODIS bands to check the consistency of the results.

In the third part, middle infrared surface reflectances, infrared emissivities and maps of directional emissivity over Southern Africa are presented and discussed. Finally, the middle infrared surface reflectance is used in a new fire detection algorithm.

2. Method

The basic concepts of the method have been formulated by Becker & Li (1990). They are (i) the use of Temperature Independent Spectral Indices of Emissivity (TISIE), derived from night-time observations, in the estimation of the surface emission in the middle infrared in the case of a day-time measurement and (ii) the use of the middle infrared surface reflectance to deduce the surface emissivity, first in the middle infrared according to Kirchhoff's law, and then in thermal infrared using again the TISIE. In this paper, we propose to improve the method by using time series of TISIE and a Bi-directional Reflectance Distribution Function (BRDF) model to apply Kirchhoff's law.

2.1. Bi-directional reflectance

Fig. 1 presents the algorithm. It is broken into five parts. We start with the spaceborne radiometric measurements and perform atmospheric corrections (1). Then, with the ground level brightness temperatures, we compute TISIE (2), retrieve middle infrared surface reflectance (3), directional emissivity (4) and finish with land surface temperature (5).

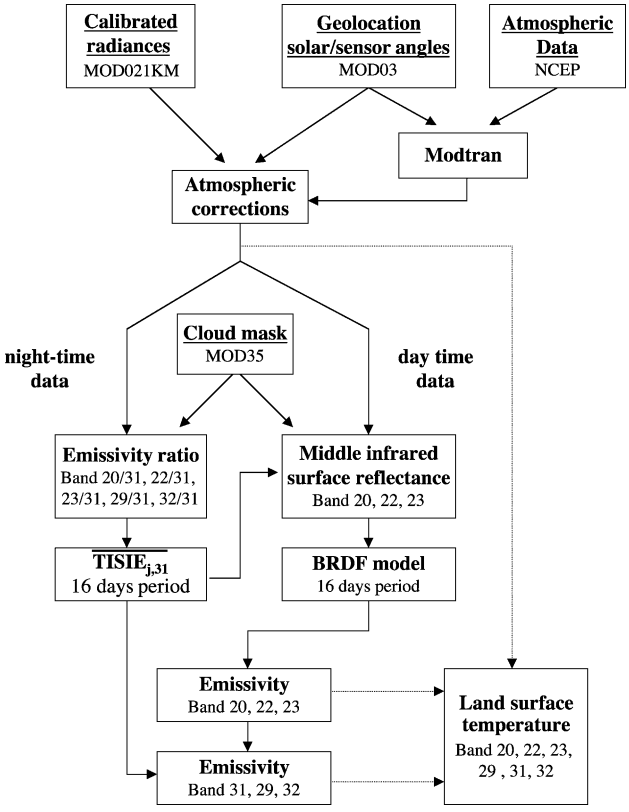

Fig. 1. General algorithm scheme.

Radiometric measurements L_i in infrared band i are expressed as a brightness temperature T using the Planck's function times the normalized spectral response of band i, f_i (λ):

$$L_i(T)\int_{\lambda_1}^{\lambda_2}\frac{f_i(\lambda)C_1}{\lambda^5[\exp(C_2/\lambda T)-1]}\mathrm{d}\lambda \tag{1}$$

$C_1 = 1.19106\times10^4$ W cm^{-2} μm^4 sr^{-1}, $C_2 = 1.43883\times10^4$ K μm and radiances are in W cm^{-2} μm^{-1} sr^{-1}.

Under cloud-free condition, the radiance measured by MODIS in emissive band i is given by:

$$L_i^* = \tau_i L_{G,i} + L_{\mathrm{atm}\uparrow i} \tag{2}$$

where $L_{G,i}$ is the surface radiance, τ_i is the total atmospheric transmittance along the target to sensor path and $L_{\mathrm{atm}\uparrow i}$ is the upwelling radiance. Inversion of the Eq. (2) is straightforward and gives access to the surface radiance.

Total atmospheric transmittance and upwelling radiance are computed using the MODTRAN (version 4.0) radiative transfer code (Acharya et al., 1998; Berk, Berstein, & Robertson, 1989). Atmospheric profiles are extracted from ancillary data provided by the National Center for Environmental Prediction (NCEP) to the MODIS users community. They cover all the troposphere, where most of the atmospheric absorbants and scatterers are present, with 27 pressure levels. They include geopotential height, temperature and relative humidity. Atmospheric data are available globally every 6 h and every degree in latitude and longitude. Regarding atmospheric constituents other than water vapor, atmospheric profiles are completed in MODTRAN using the 1976 US Standard atmospheric model. No aerosols correction is considered because either the aerosols particles are too small to impact thermal radiation according to the Mie theory, or large aerosol particle, such as dust from deserts, are not characterized to the point they could be accounted for in an nearly operational data processing scheme.

Within a MODIS granule, where an atmospheric profile is available, MODTRAN is run with the local solar and sensor angles (zenith and azimuth). Using a bi-linear interpolation, the total atmospheric transmittance and upwelling radiance are computed at the location of the MODIS pixel.

Except for day-time measurement in the middle infrared, the surface radiance is given by

$$L_{G,i} = L_i(T_{G,i}) = \varepsilon_i(\theta_v)L_i(T_s) + (1-\varepsilon_i(\theta_v))L_{\mathrm{atm}\downarrow i} \tag{3}$$

where $T_{G,i}$ is the ground level brightness temperature in band i, $\varepsilon_i(\theta_v)$ is the directional emissivity at the sensor zenith angle θ_v, T_s is the land surface temperature. $L_{\mathrm{atm}\downarrow i}$ is the downwelling atmospheric radiance, defined as $1/\pi$ times the total downwelling atmospheric irradiance as computed by MODTRAN. The term $(1-\varepsilon_i(\theta_v))L_{\mathrm{atm}\downarrow i}$ approximates the fraction of $L_{\mathrm{atm}\downarrow i}$ reflected by the surface. This term remains small compared to the emitted radiance $\varepsilon_i(\theta_v)L_i(T_s)$. We will consider it as a corrective factor.

$$C_i = 1 + \frac{(1-\varepsilon_i(\theta_v))L_{\mathrm{atm}\downarrow i}}{\varepsilon_i(\theta_v)L_i(T_s)} = \frac{1-\frac{L_{\mathrm{atm}\downarrow i}}{L_i(T_s)}}{1-\frac{L_{\mathrm{atm}\downarrow i}}{L_{G,i}}} \tag{4}$$

so that $L_{G,i} = \varepsilon_i(\theta_v)L_i(T_s)C_i$. The computation of corrective factors C_i is detailed in Nerry et al. (1998), where it is shown that uncertainties in the estimation of various corrective factors have a minor impact on final results.

In the case of day-time measurement in a middle infrared band j, the fraction of solar irradiance reflected by the surface must be added:

$$L_{G,j} = \varepsilon_j(\theta_v)L_j(T_s) + (1-\varepsilon_j(\theta_v))L_{\mathrm{atm}\downarrow j} + \rho_{b,j}(\theta_v,\theta_s,\varphi)E_{\mathrm{sun},j} \tag{5}$$

where $\rho_{b,j}$ (θ_v, θ_s, φ) is the bi-directional surface reflectivity for the sensor/solar directions, θ_s being the solar zenith angle, φ is the difference between sensor and solar azimuth angles and $E_{\mathrm{sun},j}$ is the direct solar irradiance of the surface. This quantity is computed by MODTRAN and the downwelling atmospheric radiance $L_{\mathrm{atm}\downarrow j}$ includes the diffuse solar irradiance.

Temperature Independent Spectral Indices of Emissivity (TISIE), as defined by Becker & Li (1990), are the

Table 2
$a_{j,31}$ Coefficients and $n_{j,31}$ powers for Eq. (6), together with standard error associated with $L_j(T)$

Band	$a_{j,31}$	$n_{j,31}$	RMS error	Relative error at $T=300$ K (%)
20	0.00075102	2.86792	0.00044	0.06
22	0.0014177	2.73924	0.00070	0.04
23	0.0018673	2.68211	0.00074	0.05
29	0.53117	1.28039	0.0021	0.02
32	1.11825	0.92073	0.00070	0.01

Regression is performed using a least square method with temperature ranging from 270 to 320 K by step of 0.1 K. Radiances are computed according to Eq. (1).

product of spectral emissivities in two or more bands, raised to specific powers (not necessary positive). The specific powers are given by the relation between Eq. (1) in different bands. In order to build TISIE between two bands, j and i, we perform the following regression

$$L_j(T) = a_{j,i}[L_i(T)]^{n_{j,i}} \tag{6}$$

Introducing in the above equation spectral emissivities and corrective terms defined in Eq. (4) for bands j and i, as well as Eq. (3), leads to

$$\mathrm{TISIE}_{j,i} = \frac{\varepsilon_j(\theta_v)}{[\varepsilon_i(\theta_v)]^{n_{j,i}}} = \frac{L_{G,j}}{a_{j,i}C_j}\left[\frac{C_i}{L_{G,i}}\right]^{n_{j,i}} \tag{7}$$

Hereafter, this quantity will be called emissivity ratio or TISIE. With MODIS data, we selected band 31 as a reference (i is always equal to 31) and computed emissivity ratios between all other bands considered in this work than band 31 and band j ($j=20$, 22, 23, 29 or 32). Corresponding values of $a_{j,31}$ and $n_{j,31}$ are summarized in Table 2.

A recent study has shown that emissivity ratios have small angular dependence and remain stable over several weeks (Petitcolin, Nerry, & Stoll, in press(b)). These properties are confirmed in Section 3.2 in the case of MODIS data, allowing us to build a mean emissivity ratio over a 16-day period that is representative of the actual emissivity ratio within the time period. Averaging emissivity ratios over 16 days was found to be the best method to reduce the impact of instrumental noise, approximation made in the method or errors due to uncertainties in the atmospheric data. The latter is known as the main source of error on surface radiances (Nerry et al., 1998). A mean emissivity ratio ($\overline{\mathrm{TISIE}_{j,31}}$) is computed every 16 days.

Computation of the surface emission in the middle infrared bands (the $\varepsilon_j(\theta_v)L_j(T_s)$ term) is based on the surface radiance in band 31 together with the emissivity ratio between band j and band 31. Introducing $L_{G,31}$, defined in Eq. (3), in Eq. (6) yields:

$$\begin{aligned} L_j(T_{G,31}) &= a_{j,31}[L_{31}(T_{G,31})]^{n_{j,31}} \\ &= L_j(T_s)[\varepsilon_{31}(\theta_v)C_{31}]^{n_{j,31}} \end{aligned} \tag{8}$$

Assuming that the emissivity ratio is identical during day and night, and introducing the mean emissivity ratio in Eq. (8) gives

$$\varepsilon_j(\theta_v)L_j(T_s) = \frac{\overline{\mathrm{TISIE}_{j,31}}\,a_{j,31}[L_{G,31}]^{n_{j,31}}}{C_{31}^{n_{j,31}}} \tag{9}$$

The above equation, introduced in Eq. (5), leads to

$$\rho_{b,j}(\theta_v,\theta_s,\varphi) = \frac{L_{G,j} - \overline{\mathrm{TISIE}_{j,31}}\,a_{j,31}[L_{G,31}]^{n_{j,31}}\frac{C_j}{C_{31}^{n_{j,31}}}}{E_{sun,j}} \tag{10}$$

where all terms in the right hand side are known.

2.2. Directional emissivity

Based on laboratory measurements, Salisbury, Wald, & D'Aria (1994) have shown that most of the common terrestrial surfaces follows Kirchhoff's law. This law links the directional emissivity to the directional hemispherical reflectance

$$\varepsilon(\theta_v) = 1 - \rho_h(\theta_v) \tag{11}$$

The directional hemispherical reflectance $\rho_h(\theta_v)$ is defined by Nicodemus (1965):

$$\rho_h(\theta_v) = \int_0^{2\pi}\int_0^{\frac{\pi}{2}} \rho_b(\theta_v,\theta_s,\varphi)\cos(\theta_s)\sin(\theta_s)\mathrm{d}\theta_s\mathrm{d}\varphi \tag{12}$$

In this work, we use the kernel-driven BRDF model developed by Wanner, Li, & Strahler (1995). We choose this model because it is already used to produce operationally the hemispherical reflectance from 0.47 to 2.13 μm (Strahler et al., 1999). Inversion of the BRDF model requires a minimum number of surface reflectance measurements. We chose to collect surface reflectances over 16-day periods of time and to compute the BRDF model parameters if the number of cloud-free observations is greater than or equal to six. Thus, knowing these BRDF model parameters, we are able to derive the directional hemispherical reflectance, at any view angle θ_v and therefore compute the directional emissivity. Collecting 16 days of data to compute the BRDF model parameters reduces the impact of error attached to surface reflectance on directional emissivity. The ability of the BRDF model to play the role of a noise filter has been demonstrated (Lucht, Schaaf, & Strahler, 2000). BRDF model inversions are performed every 16 days.

Once the middle infrared emissivities ε_j (θ_v) are determined, the computation of directional emissivity in thermal bands (bands 29, 31 and 32) is straightfor-

Table 3
Weather stations providing radiosonde data during the September to December 2000 time period and results of comparison of Pw (total precipitable water vapor) with NCEP data

Station name	WMO Station identifier	Elevation (m)	Latitude	Longitude	Pw (g cm^{-2}) minimum–maximum and standard deviation/NCEP
Windhoek/Eros	68110	1725	22.57°S	17.10°E	0.15–4.07, 0.24
Pietersburg	68174	1222	23.87°S	29.45°E	
Sir Seretse Khama	68240	1005	24.22°S	25.92°E	
Pretoria/Irene	68263	1500	25.92°S	28.22°E	
Bethlehem	68461	1682	28.25°S	28.33°E	
Springbok	68512	990	29.67°S	17.87°E	
Deaar	68538	1287	30.67°S	24.02°E	
Durban/Louis Botha	68588	8	29.97°S	30.95°E	
Capetown/Df Malan	68816	42	33.98°S	18.60°E	
Port Elizabeth	68842	60	33.98°S	23.60°E	
Wallops Island	72402	13	37.93°N	75.48°W	0.30–6.03, 0.36
Sterling (Wash Dulles)	72403	85	38.98°N	77.47°W	
NASA GSFC	AERONET	50	39.03°N	76.88°W	0.44–4.9, 0.32
Walker Branch	AERONET	365	35.958°N	84.287°W	

The two last lines indicate AERONET sunphotometers.

ward. The directional emissivity in band 31 is computed first:

$$\varepsilon_{31}(\theta_v) = \left[\frac{\varepsilon_j(\theta_v)}{\overline{\mathrm{TISIE}_{j,31}}}\right]^{\frac{1}{n_{j,31}}} \quad (13)$$

then the directional emissivity in bands 29 and 32 is obtained using band 31 emissivity:

$$\varepsilon_j(\theta_v) = \overline{\mathrm{TISIE}_{j,31}}[\varepsilon_{31}(\theta_v)]^{n_{j,31}} \qquad j = 29 \text{ or } 32 \quad (14)$$

Knowing the directional emissivity in six thermal bands, we are able to derive the land surface temperature T_s in each of these bands from the surface radiance (see Eq. (3))

$$L_i(T_s) = \frac{L_{G,i} - (1 - \varepsilon_i(\theta_v))L_{atm\downarrow i}}{\varepsilon_i(\theta_v)} \quad (15)$$

Because of the solar contribution in the middle infrared bands, we do not derive the land surface temperature in bands 20, 22 and 23 in the case of day-time observation. However, with night-time observation, we can compare land surface temperature obtained in six different bands. These tests (see Section 3.6) show that this method fully separates the spectral emissivity from the land surface

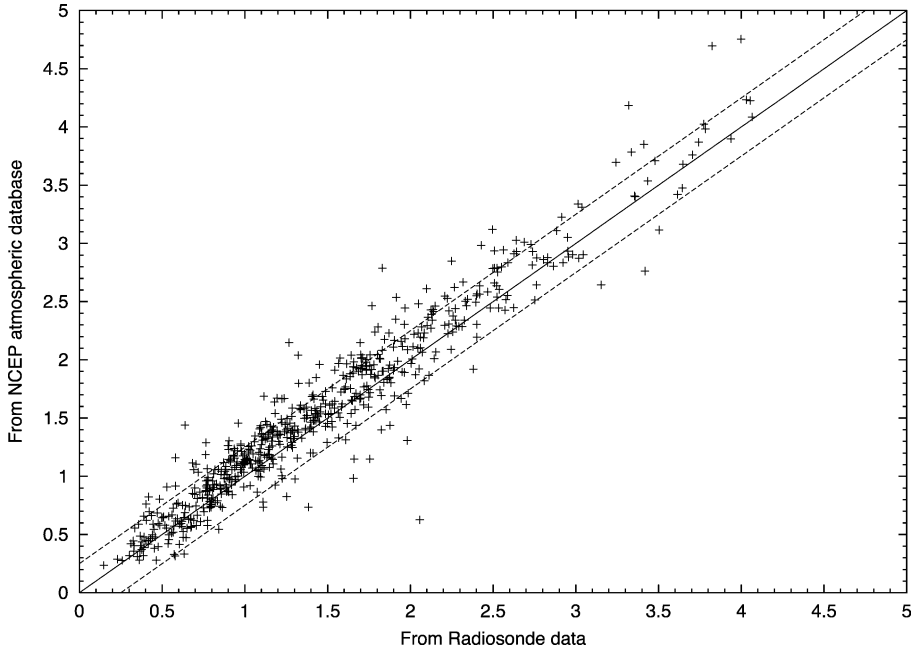

Fig. 2. Total precipitable water vapor (g cm^{-2}) derived from the NCEP database versus total precipitable water vapor derived from radiosonde data for 10 weather stations in Southern Africa (see Table 3) during September–December 2000 time period.

temperature and captures the spectral signature of the surface in the infrared.

3. Algorithm assessment

Validation of surface reflectance, emissivity or land surface temperature at the scale of MODIS observation is a very difficult task. It raises many issues such as scaling, surface homogeneity or the definition of the quantities themselves. Such problems are not addressed in this paper. In the following sections, we describe a set of comparisons and tests for each step of the method. Our algorithm assessment is based on a previous analytical sensitivity study of the middle infrared emissivity (Nerry et al., 1998), extended to the thermal infrared emissivity by (Petitcolin et al., in press(b)).

3.1. Atmospheric corrections

This section is dedicated to the assessment of the atmospheric corrections. Two types of test are performed: one

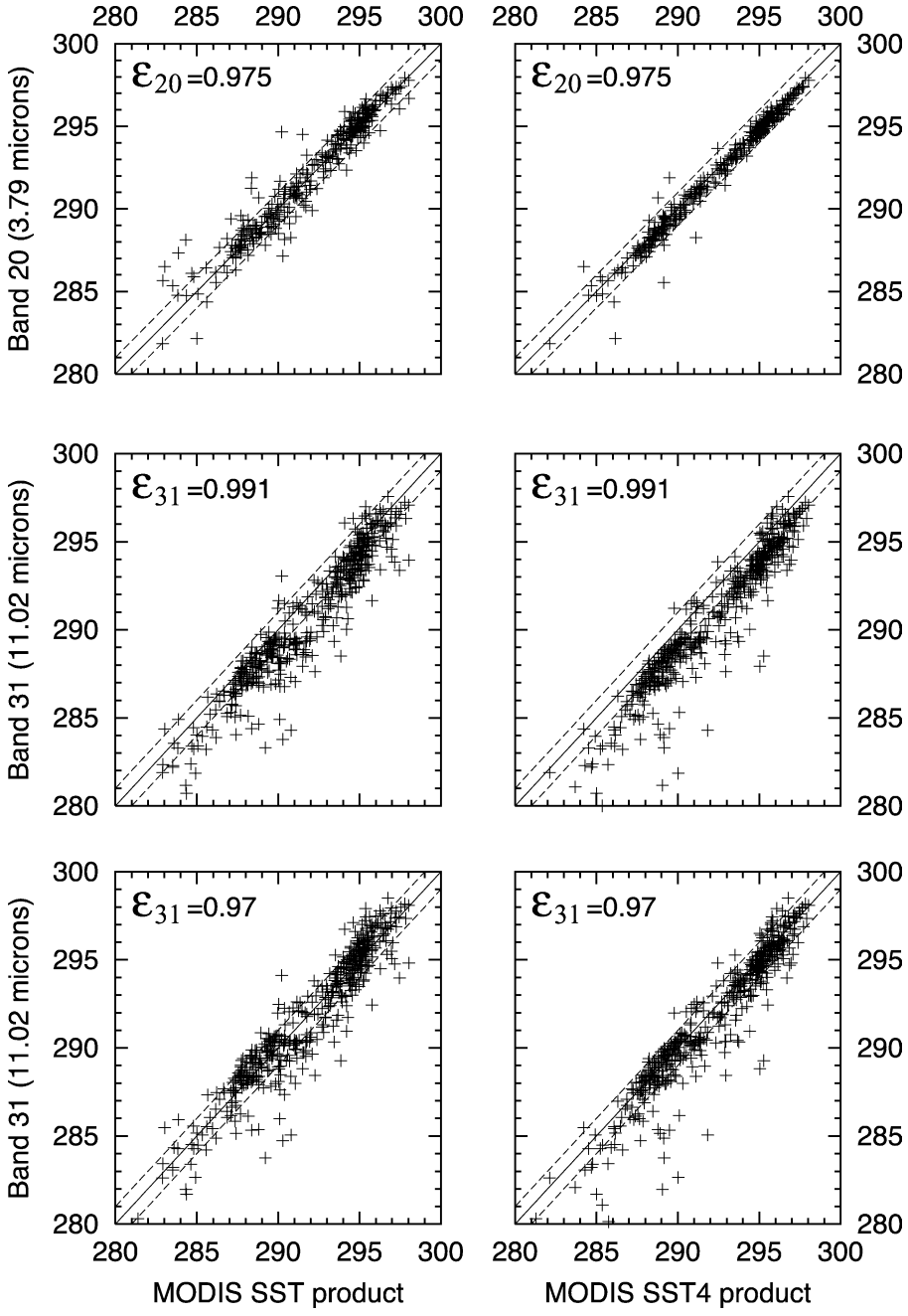

Fig. 3. Surface temperature (K) in bands 20 and 31 versus MODIS SST products. For band 31, reference emissivity ($\varepsilon_{31}=0.991$) and adjusted emissivity ($\varepsilon_{31}=0.97$) have been introduced in Eq. (15).

Table 4
Comparisons between surface temperatures obtained in MODIS bands 20, 22, 23, 29, 31 and 32 using Eq. (15) and MODIS SST products over sea

Band	20	22	23	29	31	32	29	31	32
Emissivity	0.975	0.9755	0.976	0.985	0.991	0.986	0.97	0.97	0.96
Standard deviation/SST	0.91	0.83	0.81	1.59	1.61	2.24	1.30	1.23	1.81
Standard deviation/SST4	0.58	0.29	0.62	1.79	1.85	2.41	1.41	1.29	1.80

on the atmospheric data, and the other on the surface radiances.

Nerry et al. (1998) show that the accuracy of middle infrared reflectance retrieval is limited by the uncertainties of the atmospheric data, particularly in the water vapor profile. To evaluate the NCEP data, we computed the atmospheric profile over several weather stations (see Table 3) using a simple bi-linear spatial interpolation of surrounding NCEP atmospheric profiles. Then, we computed the total precipitable water vapor and compared it to the radiosonde data. Radiosonde data are extracted from the FSL/NCDC Radiosonde Data Archive (http://raob.fsl.noaa.gov/). As this study is focused on the southern part of Africa, a first comparison is performed over 10 stations in this region during September–December 2000 time period. Values of total precipitable water vapor derived from the NCEP database are in good agreement with those from radiosonde data (see Fig. 2), with a standard deviation of 0.24, as given in Table 3. However, because this study occurs during the dry season in Southern Africa, the range of total precipitable water vapor is limited (0.15–4.0 cm). Therefore, additional tests were performed over two weather stations of the East coast of the United States during the same time period. Values of total precipitable water vapor are in good agreement over a larger range (0.3–6.0 cm), with standard deviation less than 0.36. Additional tests were performed using an independent source of total precipitable water vapor measurement with similar results. The AErosol RObotic NETwork (AERONET) program is a network of sunphotometers (Holben et al., 1998). Its primary goal is to assess aerosol optical properties, but total precipitable water vapor is also retrieved using sunphotometer records in the 940-nm band width an accuracy comparable to that of radiosonde (Halthore, Eck, Holben, & Markham, 1997). Two sunphotometer sites have been selected (see Table 3) and values of total precipitable water vapor during the September–December 2000 time period have been compared to NCEP data. They agree well with a standard deviation of 0.32. In conclusion, these tests show that the NCEP database suits our needs in terms of atmospheric profile accuracy. Its spatial and temporal sampling allow us to perform single band atmospheric corrections on a systematic and global basis.

Oceans are large homogeneous surfaces at the scale of MODIS observations. Emissivity of water is well characterized, allowing us to apply Eq. (15) in order to derive a surface temperature. Emissivity values introduced in Eq. (15) for bands 20, 22, 23, 29, 31 and 32 are set to 0.975, 0.9755, 0.976, 0.985, 0.991 and 0.986, respectively. They are based on the ASTER spectral library (http://speclib.jpl.nasa.gov) in addition to Masuda, Takashima, & Takayama

Table 5
Description of the four test areas

Reference	Latitude	Longitude	IGBP class	Description
A	24.84°S	13.25°E	Water bodies	ocean
B	25.71°S	19.59°E	Cropland/natural vegetation mosaic	farms, grasses and shrubs
C	26.16°S	15.04°E	Barren or sparsely vegetated	desert
D	26.31°S	21.04°E	Open shrubland	shrubs with bare soil

Area size is 0.01 × 0.01° in latitude and longitude.

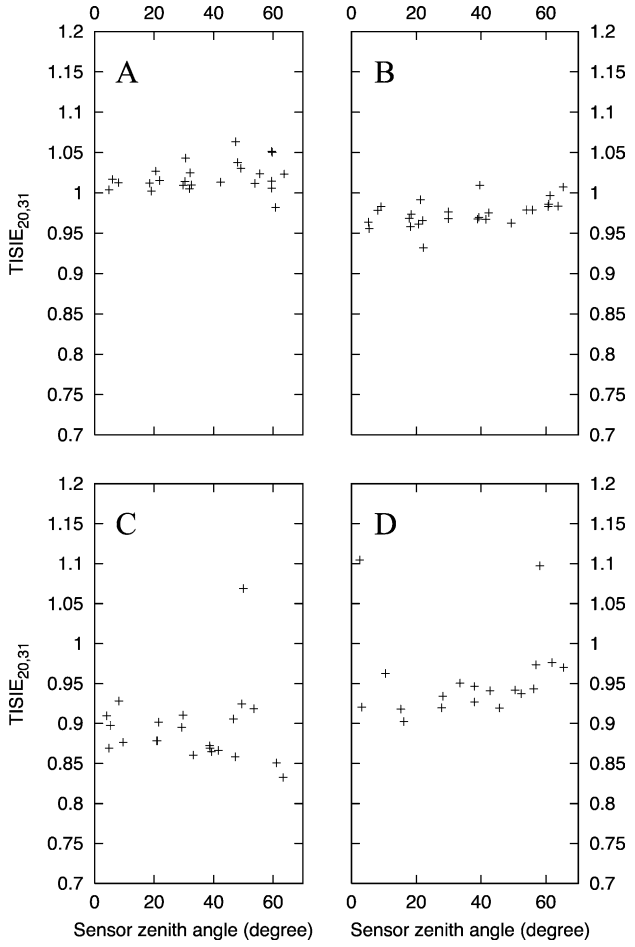

Fig. 4. Night-time emissivity ratio band 20/band 31 $TISIE_{20,31}=(\varepsilon_{20}(\theta_s))/(\varepsilon_{31}^{2.86792}(\theta_s))$ for the four test areas (A, B, C and D) described in Table 5 and for a period of time starting August 20th, 2000 and ending October 24th, 2000.

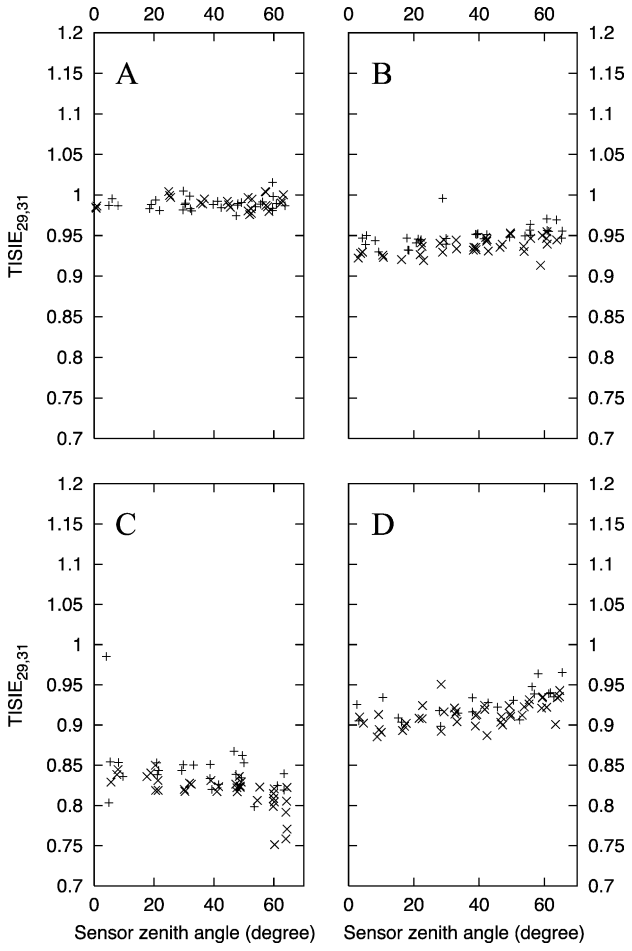

Fig. 5. Night-time emissivity ratio (+) and day-time emissivity ratio (×) band 29/band 31 $TISIE_{29,31}=(\varepsilon_{29}(\theta_s))/(\varepsilon_{31}^{1.28039}(\theta_s))$ for the four test areas (A, B C and D) described in Table 5 and for a period of time starting August 20th, 2000 and ending October 24th, 2000.

(1988), Salisbury & D'Aria (1994), Snyder et al. (1998). Angular variations of the water emissivity are too small to have any significant impact on the surface temperature and are not considered here. The surface temperature can be compared to the MODIS SST product (Brown et al., 1999). Even if the quality of this product is not optimal at the time of this test, it is worth comparing our approach regarding atmospheric corrections with the traditional split-window technique. Two SST products are available: one using MODIS bands 31 and 32, and the other using MODIS bands 20, 22 and 23, called the middle infrared SST, or SST4. Night-time surface temperature in bands 20, 22, 23, 29, 31 and 32 for clear sky conditions and the MODIS SSTs have been collected over 158 locations around Southern Africa, starting August 28th, 2000 and ending September 13th, 2000. Surface temperatures are plotted in Fig. 3 for bands 20 and 31. Results in bands 22 and 23 [resp. bands 29 and 32] are similar to those in band 20 [resp. band 31]. Table 4 summarizes the statistics between the two data sets. In general, surface temperatures are in good agreement with MODIS SST products. Standard deviations are less than 1° for middle infrared bands, down to 0.29 for band 22 against SST4. Standard deviations for bands 29, 31 and 32 are slightly higher, with a bias of about 1° visible in Fig. 3 for band 31. Such bias is removed by adjusting the emissivity value, reducing by 0.4 to 0.8 the standard deviations. Adjusted emissivity in the thermal infrared bands is lower than those found in the literature. This could be explained by the presence of suspended sediments or other particles, or foam, at the ocean–atmosphere interface. Impact of sediments or foam on emissivity of water is much more important in thermal infrared than in middle infrared (Salisbury & D'Aria, 1994).

3.2. Assessment of the hypothesis on emissivity ratios

The middle infrared surface reflectance retrieval, as described above, relies on three types of hypotheses with regard to the emissivity ratios: (1) computing a mean emissivity ratio over 16-day period, we assumed the TISIE indices to be stable over the time period; (2) to be independent of the view angle; (3) emissivity ratios between middle infrared bands and band 31 are assumed to be equal for night-time and day-time observations. Analysis of the time series of emissivity ratio offers the possibility to assess hypotheses (1) and (2). The third assumption cannot be directly evaluated but we analyze here day and night emissivity ratios between bands 29 (8.53 μm) and 31.

Emissivity ratios over Southern Africa have been computed for the period of time starting August 20th, 2000 and ending October 24th, 2000. Coordinates and description of four test areas are summarized in Table 5. Four different types of natural surface are presented: water (A), vegetated surface (B), arid (C) and semi-arid (D). All emissivity ratios between bands 20 and 31 collected over each area are plotted against the satellite view angle in Fig. 4. Below 55° of view angle, no significant angular variation of the

Table 6
Statistics of middle infrared surface reflectances in bands 20, 22, and 23 over water

Middle infrared surface reflectance (%)	Band 20		Band 22		Band 23	
	Ocean	Lake	Ocean	Lake	Ocean	Lake
Average	1.28	0.53	1.24	0.07	1.41	− 0.40
Standard deviation	1.44	0.57	1.48	1.52	1.73	2.24
Minimum	− 0.40	− 1.60	− 0.60	− 4.60	− 1.67	− 7.07
Maximum	8.78	2.71	7.72	6.90	7.77	8.31
Observations	390	67	501	92	488	89

emissivity ratios is visible. Above 55°, uncertainties in the atmospheric corrections become significant. Moreover, the higher the view angle, the larger the target, while still centered on the same location. Even if we selected test areas surrounded by pixels falling in the same class of land cover type, the small variations we recorded might be related to the increasing size of the MODIS pixel with view angle. Fig. 4 also shows that the emissivity ratios are relatively stable within a 2-month period of time. Emissivity ratios between bands 22 and 31 or between bands 23 and 31 give similar results. The TISIE are spread within 0.03 around a mean value. As they are stable over time and view

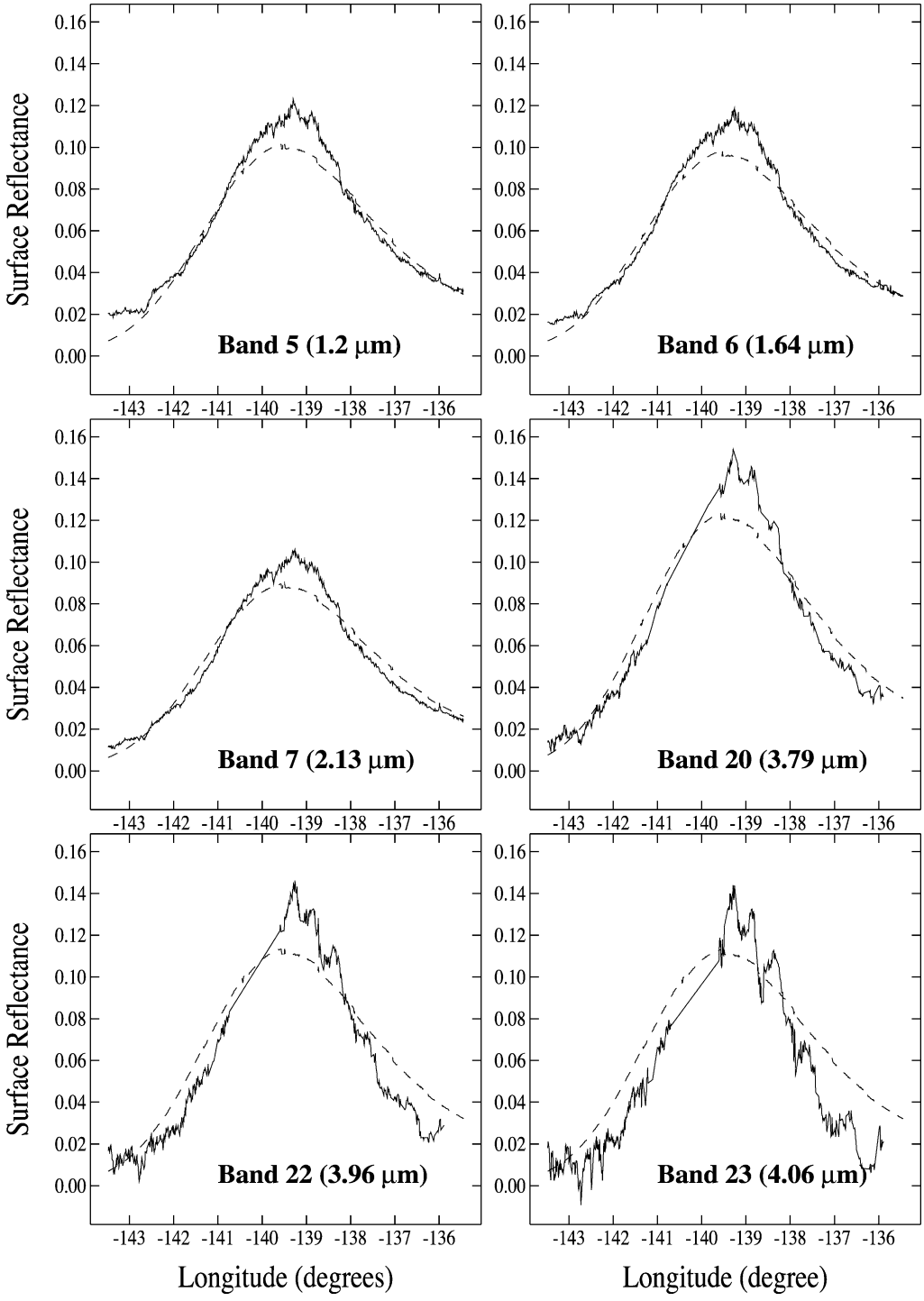

Fig. 6. Measured (solid line) and model computed (dashed line) surface reflectances in MODIS bands 5, 6, 7, 20, 22 and 23 across a glitter (October 23rd, 2000, 20:05 GMT, transect centered on 2.33° South, 139.48° West).

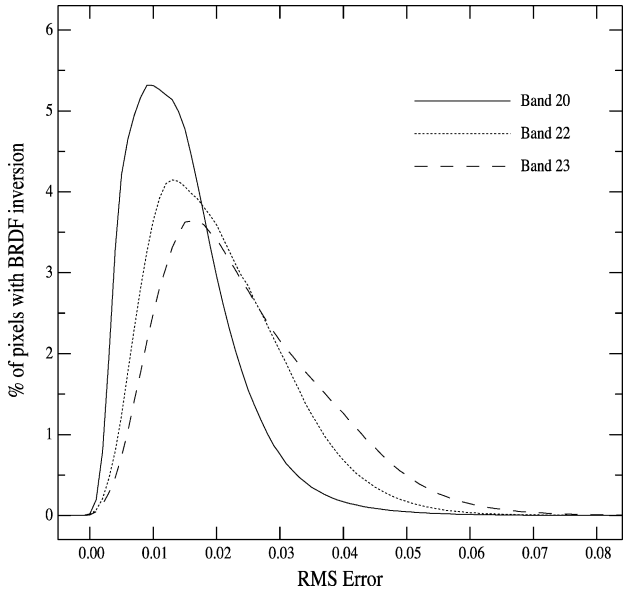

Fig. 7. Histogram of the root mean-square-error between surface reflectance measurements and BRDF model results for MODIS bands 20, 22 and 23, 16-day time period starting September 13th, 2000 over Southern Africa.

angles, a better signal to noise ratio is obtain by averaging TISIE over 16 days of measurements. The few outliers in Fig. 4 are due to cloud contamination of the pixels.

Because of the solar reflection in the case of day-time observation, emissivity ratios between middle infrared bands and band 31 cannot be derived from day-time images. However, emissivity ratios between bands 29 and 31 can be achieved in both cases. From a spectral point of view, this is the closest emissivity ratio we can derive with both day-time and night-time data. These emissivity ratios for the test areas and the time period mentioned above are plotted against view angle in Fig. 5. It is worth noting that emissivity ratios between bands 29 and 31 show a good angular and temporal stability as well. Day-time and night-time data are well mixed in all cases, showing that the assumption of an emissivity ratio insensitive to day–night cycle is valid for $TISIE_{29,31}$.

3.3. Validation of middle infrared surface reflectance

For validation purpose, we need large and homogeneous targets where the middle infrared surface reflectance is known. Oceans and inland water bodies match our needs. According to the optical properties of water in the middle infrared spectral region (Hale & Querry, 1973), the surface reflectance of water is very close to zero, sun-glint conditions excepted. In order to perform validations for a extended range of surface reflectance, we also compared measured and model-computed middle infrared surface reflectances in one case of sun-glint.

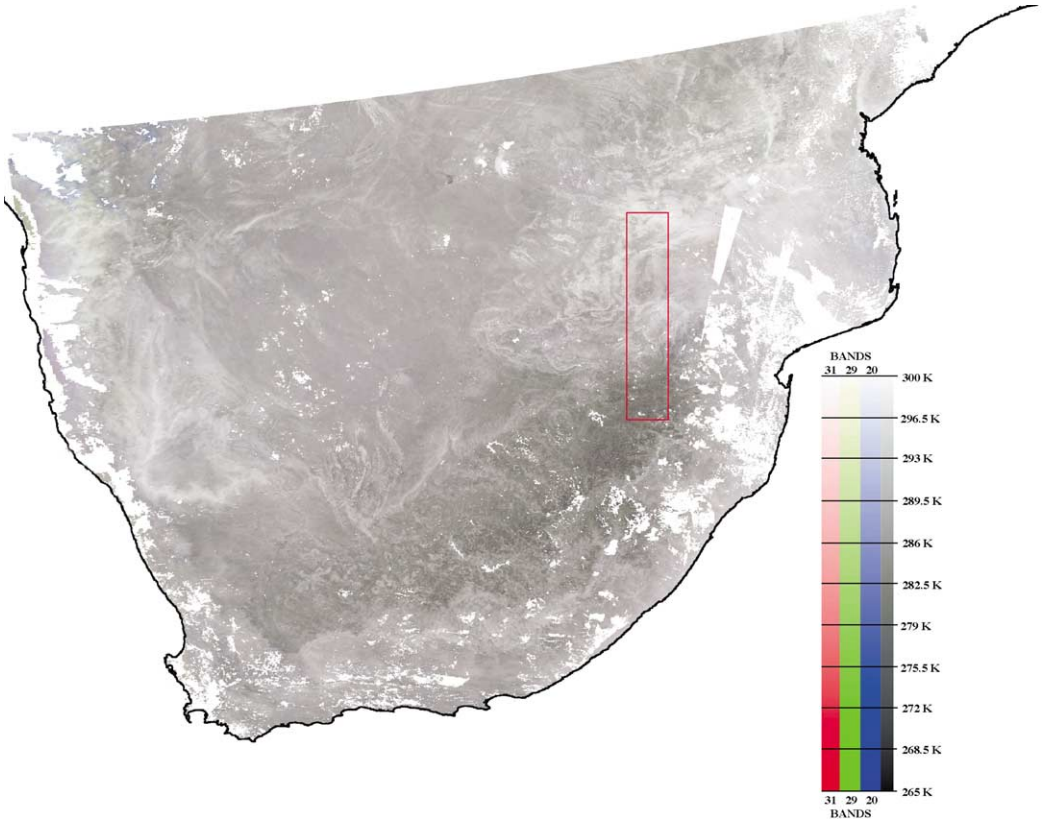

Fig. 8. Surface temperature in MODIS band 20 (blue), 29 (green) and 31 (red) of Southern Africa for September 1st, 2000 at 21:10 GMT (night-time data).

Middle infrared surface reflectances over 23 areas off the Atlantic Southern African shore and over four lakes (Bangweulu and Kariba in Zambia, Malawi in Tanzania and Cahora Bassa in Mozambique) for the period of time starting August 20th, 2000 and ending October 24th, 2000 are collected. Statistical analysis of these surface reflectances is summarized in Table 6. Average values are less than 1.5% (or 0.015 in reflectance unit) for all bands. Standard deviations are lower in band 20, and increase with the wavelength. This is due to a stronger signal (the fraction of solar irradiance reflected by the surface) in band 20 than in band 22 or 23. In general, minimum and maximum values are reasonable. Very low or very high surface reflectances are sometime retrieved when NCEP data are not representative of the atmospheric conditions in the test area or when clouds are contaminating the retrieval. Negative values of

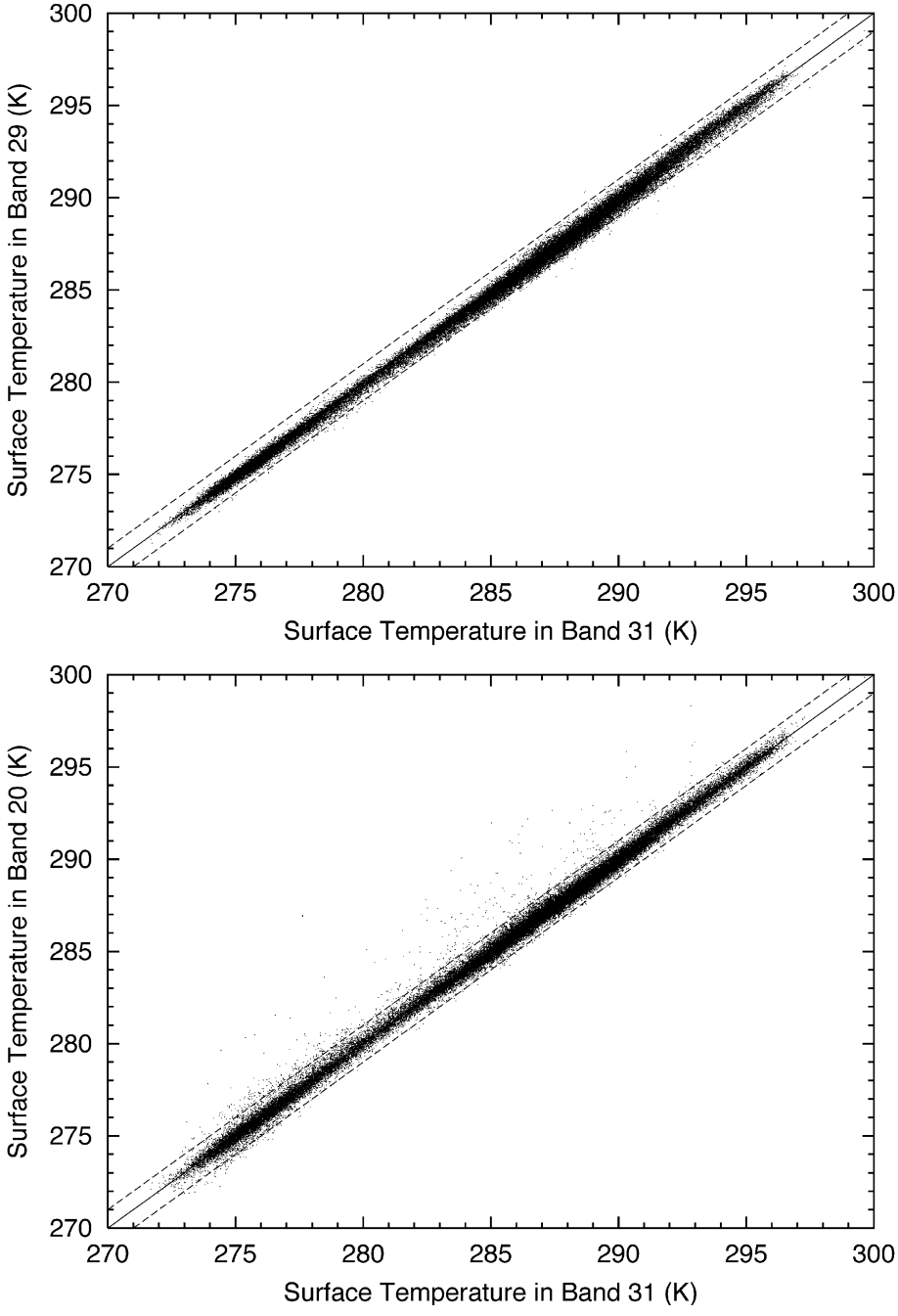

Fig. 9. Surface temperature in band 20 (lower plot) and in band 29 (upper plot) versus surface temperature in band 31 computed within the area delimited by the red rectangle in Fig. 8.

surface reflectance correspond to an overestimation of the surface thermal emission in the middle infrared band (see Eq. (10)). Based on these results, we assess the middle infrared surface reflectances accuracy to be of the order of 0.015 at low level.

Validation of higher surface reflectance is achieved by comparing retrieved water surface reflectance under glint conditions with the results of the Cox and Munk model (Cox and Munk, 1954). This model is implemented in 6S (Vermote, Tanré, Deuzé, Hermann, & Morcrette, 1997). We modified the existing code to extend its capabilities up to 4.2 μm and introduced the sensor spectral response of MODIS bands 20, 22 and 23. We selected a case over the Pacific Ocean (around 2.33° South and 139.48° West) and retrieved the middle infrared surface reflectance for the MODIS granule recorded October 23th, 2000 at 20:05 GMT. The Cox and Munk model shows that the ocean surface reflectance under sun-glint conditions is very sensitive to the wind speed and to a lesser extent to the wind direction. Wind speed and wind direction have been extracted from the NCEP atmospheric database. Fig. 6 compares measured and modelled surface reflectances along a transect perpendicular to the glint pattern at various wavelengths. Surface reflectances in bands 5, 6 and 7 are extracted from the MOD09 surface reflectance product. Along the transect, results in bands 5, 6, 7 and 20

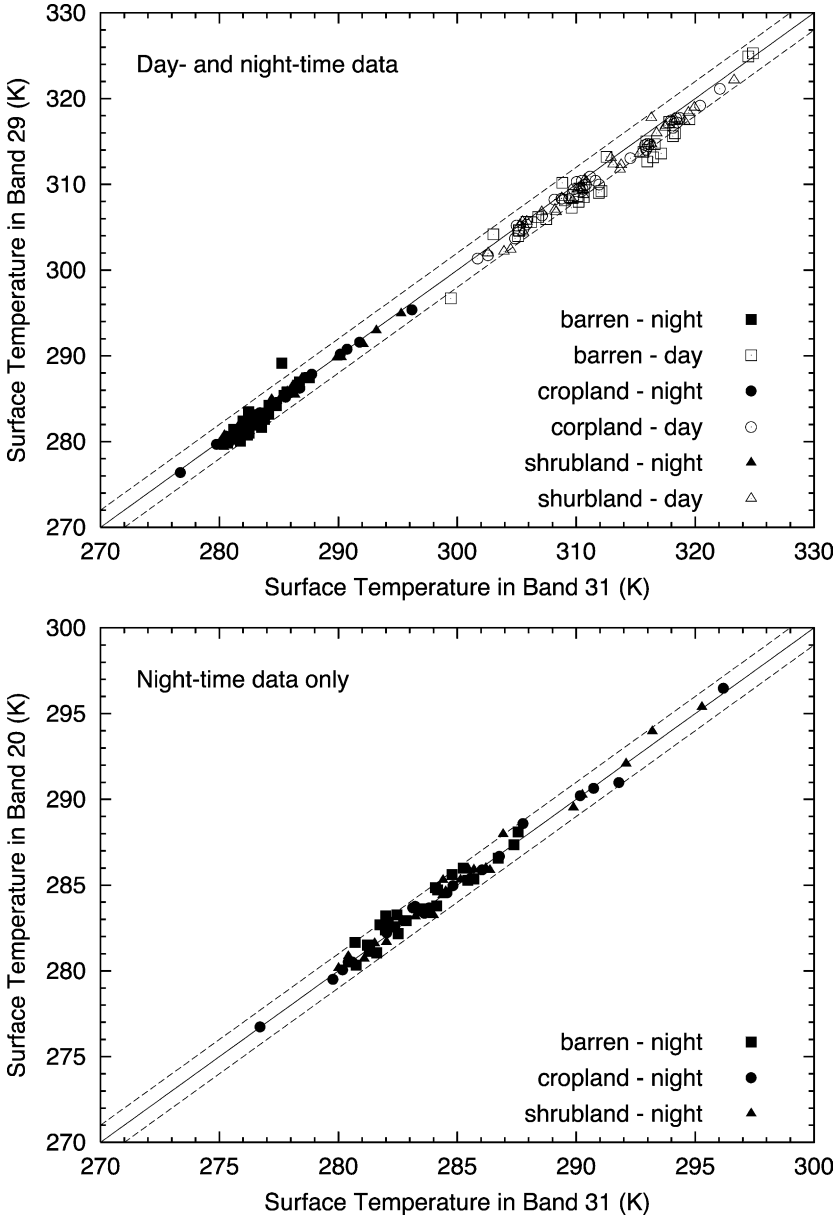

Fig. 10. Surface temperature in band 20 (lower plot) and in band 29 (upper plot) versus surface temperature in band 31 computed over the three land test areas defined Table 5 during time period starting August 20th, 2000 and ending October 24th, 2000.

are in good agreement with model computations, except for the largest reflectances where the model underestimates the surface reflectance. Results in bands 22 and 23 are not so good but still within ± 0.015 compared to model computations.

3.4. Assessment of the BRDF inversion

The BRDF model inversion is the key to deriving the directional emissivity from surface reflectance measurements in middle infrared through Kirchhoff's law. This inversion is performed on a pixel by pixel basis. BRDF model inversion is assessed using the root-mean-square-error (RMSE) between measured surface reflectances and results of the model. Fig. 7 shows the histogram of these RMSE for all land pixels of Southern Africa (south of the 10°S parallel) for surface reflectance measurements collected during the 16-days period starting September 13th, 2000. Ninety five percent of BRDF model inversions in band 20 [resp. 22 and 23] have an RMSE below 0.03 [resp. 0.04 and 0.05]. This number decreases to 0.025 [resp. 0.035 and 0.043] for 90% of the inversions. This shows that the reciprocal RossThick–LiSparse semi-empirical model proposed by Lucht et al. (2000) reasonably describes the middle infrared surface BRDF. Not surprisingly, better fits are obtained in band 20 than in band 22 or 23.

3.5. Comparison of emissivity at 11 μm

As the BRDF model inversion is performed using surface reflectances in middle infrared bands 20, 22 and 23, directional emissivities in these three bands are independently derived. Each middle infrared emissivity, together with average emissivity ratios $\overline{\mathrm{TISIE}_{j,31}}$, $j = 20,\ 22$ or 23, gives access to emissivity in band 31 (see Eq. (7)). It is worth comparing the results of the three different ways to obtain emissivity at 11 μm. A temporal analysis is performed with seven 16-day periods starting on days 233, 241, 249, 257, 265, 273 and 281 of year 2000. For each 16-day period, average emissivity ratios and BRDF model parameters have been computed for the three land test areas (B, C and D) defined in Table 5. Then, nadir emissivity in band 31 is computed for each 16-day period. The overall mean emissivity in band 31 for areas B, C and D are 0.967, 0.937 and 0.969, respectively. Emissivities in band 31 derived using bands 22 and 23 agree with emissivities derived using band 20 within 0.0063 and 0.0086, respectively (standard deviations), and emissivities in band 31 derived using 22 agree with emissivities derived using band 23 within 0.0063. These results show a very good coherence of the emissivities in band 31, suggesting it is retrieved with an error of less than 1%.

In the data processing chart shown in Fig. 1, only the emissivity in band 31 computed from band 20 is produced. Our choice was motivated by the conclusions of the two preceding sections.

3.6. Comparison of land surface temperatures

A final test is to compare the land surface temperatures obtained in six MODIS bands by Eq. (15). Theoretically, the land surface temperature should be identical in all bands, showing evidence of the emissivity/LST separation. For that purpose, we performed one regional test with a night-time scene over Southern Africa and one temporal test for the three land test areas described in Table 5 starting August 20th, 2000 and ending October 24th, 2000.

MODIS granule starting September 1st, 2000 at 21:10 GMT over Southern Africa is mostly cloud-free. Because it is a night-time acquisition, land surface temperatures in middle infrared bands (20, 22 and 23) have been retrieved, as well as in thermal bands (29, 31 and 32) except for cloud and sea pixels. In order to compare LST in different bands, Fig. 8 is a Red–Green–Blue color image with surface temperatures in bands 20 [resp. 29 and 31] scaled to the blue [resp. green and red] channel. Areas in white are either ocean or cloudy or missing BRDF model parameter or missing mean emissivity ratio. If the temperatures are exactly the same in the three bands, Fig. 8 should be a black and white image. Indeed, this figure is close to a black and white image with a light touch of green at the top. Green tint corresponds to a surface temperature in band 29 higher than those in bands 20 and 31, but only by a few tenths of a degree. Small areas in green are visible on the left side of Fig. 8. At the edge of the swath, where the sensor zenith angle is above 60°, the accuracy of directional emissivities decreases rapidly, leading to differences between surface temperatures of several degrees. Surface temperatures in the area delimited by the red rectangle in Fig. 8 are compared in Fig. 9. This part of the scene includes large variations of temperature, in the order of 25 K. For most of the pixels, land surface temperature difference is less than 1°. We obtain similar results with bands 22, 23 and 32.

Surface temperatures in bands 20, 29 and 31 for the three land test areas during August 20th–October 24th, 2000 time period, are compared in Fig. 10. Surface temperatures in these three bands agree well with each other.

Table 7 summarizes the standard deviations between the land surface temperatures retrieved in the different bands for

Table 7
Standard deviation between land surface temperatures computed in MODIS bands 20, 22, 23, 29, 31 and 32

	Band	Temporal analysis					
		20	22	23	29	31	32
Regional analysis	20	×	0.45	0.51	0.53	0.40	0.49
	22	0.59	×	0.54	0.56	0.47	0.55
	23	0.81	0.60	×	0.44	0.52	0.62
	29	0.85	1.19	1.12	×	0.36	0.44
	31	0.46	0.77	0.85	1.29	×	0.20
	32	0.61	0.89	0.96	1.46	0.59	×

Upper right half of the table summarizes results within the area delimited by the red rectangle in Fig. 8. Lower left half of the table summarizes results for the three land test areas (see Table 5) and for a time period starting August 20th, 2000 and ending October 24th, 2000.

both regional and temporal analysis. They are always better than 1.5 K and most of them are within 0.4 and 1 K. These results show a great coherence of the land surface temperatures retrieved at different wavelengths. This means that the spectral emissivity is totally separated from the land surface temperature. According to these results, the land surface temperature accuracy is of the order of 1°.

4. Results and applications

4.1. Middle infrared surface reflectances

In this section, we analyze surface reflectances in MODIS bands 20, 22 and 23 for the two test areas C and D described in Table 5. Figs. 11 and 12 show the surface reflectances collected during the 16-day period starting August 20th, 2000 as a function of sensor zenith angle

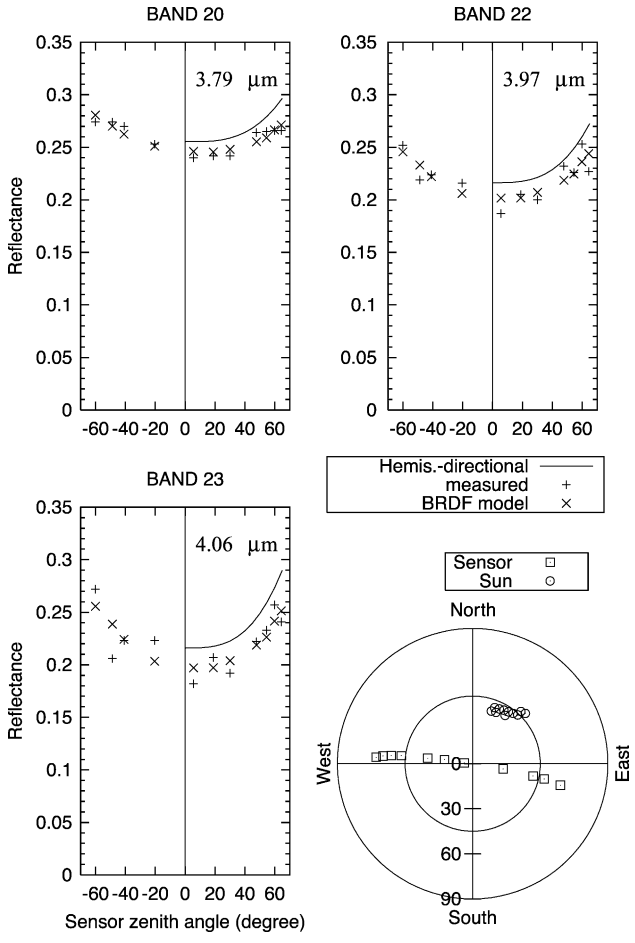

Fig. 11. Middle infrared surface reflectance, BRDF model and hemispherical directional reflectance in MODIS band 20 (top left), 22 (top right) and 23 (bottom left) for test area C (IGBP class 'Barren or sparsely vegetated', see Table 5). Bottom right polar plot indicates sun and sensor directions.

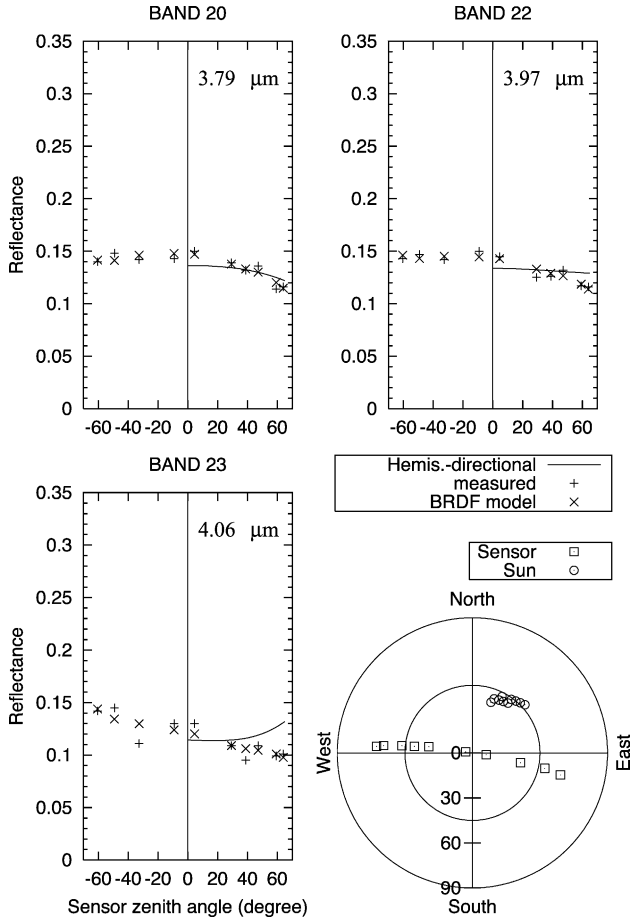

Fig. 12. Middle infrared surface reflectance, BRDF model and hemispherical directional reflectance in MODIS bands 20 (top left), 22 (top right) and 23 (bottom left) for test area D (IGBP class 'Open Shrubland', see Table 5). Bottom right polar plot indicates sun and sensor directions.

and the observation geometry. The overpass local time of the TERRA platform is around 10:30 in the morning. As shown in the polar plots of Figs. 11 and 12, all target-to-Sun directions fall in the North–East quarter of the polar plot because they correspond to morning observations in the Southern Hemisphere. All observations are in an intermediate plane between the principal plane and the perpendicular plane, somewhat closer to the perpendicular plane. The negative value of sensor zenith angle corresponds to backscattering, i.e. sun and sensor are in the same half (East) of the polar plot. A solid line represents the hemispherical directional reflectance, equal to $1-\varepsilon_f(\theta)$.

Test area C has been selected as representative of bare soils. As shown in Fig. 11, middle infrared reflectances are large, above 0.2, and increase with the sensor zenith angle. These results agree with laboratory measurements (Salisbury & D'Aria, 1994; Snyder, Wan, Zhang, & Feng, 1997). Similar angular variations of surface reflectance have been measured by Nerry et al. (1998) with AVHRR data. In the current observation plan, middle infrared surface reflectance increases by 10% to 20% as sensor

zenith angle goes from 0 to 60°. This type of surface does not behave like a lambertian surface. The BRDF model fits successfully all reflectances and the hemispherical directional reflectance increases (the directional emissivity decreases) significantly as the sensor zenith angle increases. Surface reflectances in bands 20, 22 and 23 are similar. Reflectances at 3.79 μm are slightly higher than those at 3.97 and 4.06 μm, with weaker angular variations. They appear to be less noisy, as already mentioned in Section 3.3.

Test area D shows different results because of the presence of sparse vegetation (see Fig. 12). Middle infrared surface reflectances are lower than those recorded over area C, with values below 0.15. Angular variations are weak. As the sensor zenith angle increases, reflectances in the forward scattering half plan decrease by a few percent and reflectances in the back scattering half plan remain stable or show a slight increase. In the same observation plane, similar angular behavior is recorded for vegetation covered surfaces in visible or near-infrared spectrum or in middle infrared with AVHRR (Petitcolin et al., in press(a)). However, hot-spot phenomenon, typical of vegetation-covered surfaces, does not appear in the current observation plane.

4.2. Spectral signature in infrared spectrum

With this method, the MODIS instrument gives access to the emissivity at 3.79, 3.97, 4.06, 8.53, 11.02 and 12.03 μm. In this section, we focus on the spectral signature of the three land test areas defined in Table 5. An analysis of the infrared spectral signature at a regional scale is conducted in the next section.

At first glance, Fig. 13 shows similar signature for areas B and D, with higher emissivity than for area C. With the latter being representative of bare soil, we see the impact of vegetation on infrared signature. In the middle infrared, it is worth noting that emissivity below and above 4 μm is similar for areas B and D, whereas they show significant variation for area C. The latter presents very low emissivity around 8.5 μm (band 29), corresponding to the strong absorption of silicates in this spectral region. Emissivity difference between 11 and 12 μm is also more important for area C (0.023) than for areas B and D (0.009 and 0.006, respectively). This emissivity difference has an impact on the land surface temperature retrieval using the split-window technique (Becker, 1987).

With regard to the angular variations of the spectral emissivity, area C shows a significant decrease of the emissivity when the sensor zenith angle increases, whereas such variations are small for area B and negligible in the case of area C. Angular variations of the emissivity are similar whatever the wavelength in the infrared spectrum. In fact, angular variations found in band 20 are reproduced in bands 29, 31 and 32 because emissivity ratios are assumed to be independent of the sensor zenith angle. Regarding

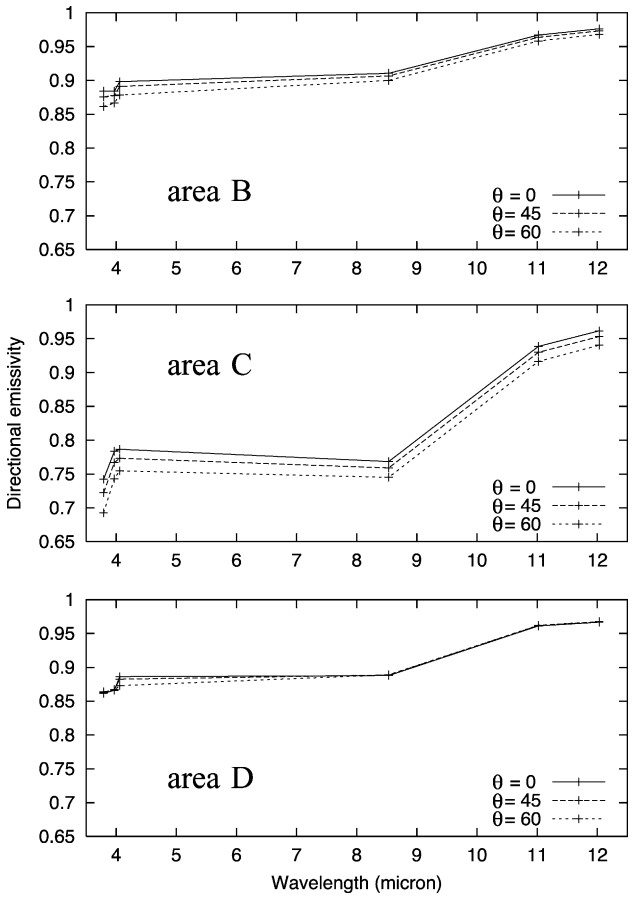

Fig. 13. Infrared spectral signature of the three land test areas defined in Table 5. Directional emissivity $\varepsilon_i(\theta)$ in MODIS bands 20, 22, 23, 29, 31 and 32 is derived for three sensor zenith angles (0°, 45° and 60°).

angular variations of spectral emissivity, the assumption of emissivity ratios independent of the sensor view angle in Eq. (7) leads to

$$\frac{\varepsilon_i(\theta_1)}{\varepsilon_i(\theta_2)} = \left[\frac{\varepsilon_j(\theta_1)}{\varepsilon_j(\theta_2)}\right]^{\frac{1}{n_{j,i}}} \tag{16}$$

Angular variations are not identical over the infrared spectrum, being scaled by the $n_{j,i}$ powers. This mechanism is illustrated in Fig. 13 in the case of test area D. As negligible angular variations of emissivity in band 20 are recorded, emissivity in bands 29, 31 and 32 show no angular variation. Angular variations of emissivity on band 23 appear to be an artifact because results in band 20 are confirmed by the results in band 22. We are confident in this characterization of the spectral directional emissivity for two reasons. First, in the middle infrared, angular variations of directional hemispherical reflectance (equal to $1-\varepsilon(\theta)$) in bands 22 and 23 are very similar to those recorded in band 20, as shown in Figs. 11 and 12. It should be reemphazised that surface reflectances in bands 20, 22 and 23 are independently retrieved. Second, we checked that differences between land surface temperatures derived in all six MODIS bands are independent of the sensor zenith angle up to 55°.

4.3. Mapping emissivity

MODIS data from August 20th to October 22nd, 2000 over Southern Africa (south of the 10° south parallel) have been processed. The processing scheme provided us with BRDF parameters in bands 20, 22 and 23 and a set of emissivity ratios for seven 16-day periods. From this dataset, we derived nadir emissivity in all six MODIS bands for each period. Fig. 14 shows the results for the 16-day period starting August 20th, 2000. Emissivity retrieval has been completed for most of the region. Black color indicates that emissivity was not derived because of either BRDF model parameters or emissivity ratios were not available due to the lack of cloud-free observation during this 16-day period. The percentage of missing data increases after August 20th as we go from the dry season to the wet season over Southern Africa. Ocean pixels were not processed because the BRDF model is not adapted to this type of specular

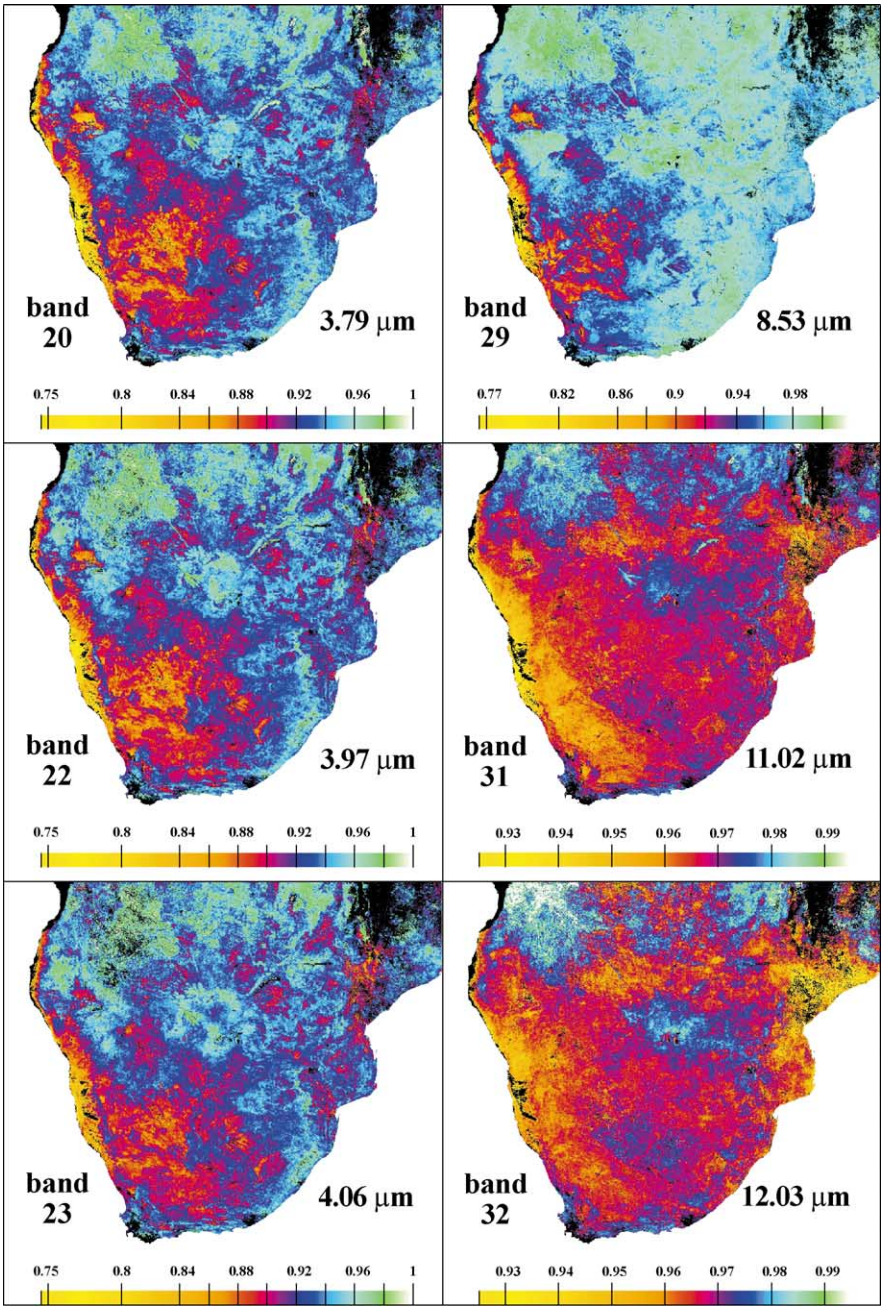

Fig. 14. Map of spectral emissivity at nadir in MODIS bands 20, 22, 23, 29, 31 and 32 over Southern Africa (south of the 10° South parallel) for the 16-day period starting August 20th, 2000.

surface. This part of the African continent offers a large diversity of surface types, from the Namib desert along the west coast to the dense vegetation covered areas of the Kwanza and Zambesi hydric basins in the North. Various types of sparsely vegetated areas, shrubland and savanna are present within the Kalahari desert and the surrounding area.

In Fig. 14, nadir spectral emissivity presents a different range of variation depending on the wavelength. Middle infrared emissivity (bands 20, 22 and 23) ranges from 0.75 for bare soils (Namib Desert) to unity for dense vegetation. Emissivity at 8.53 μm is higher over bare soils and reaches unity as the density of vegetation increases. Emissivity in

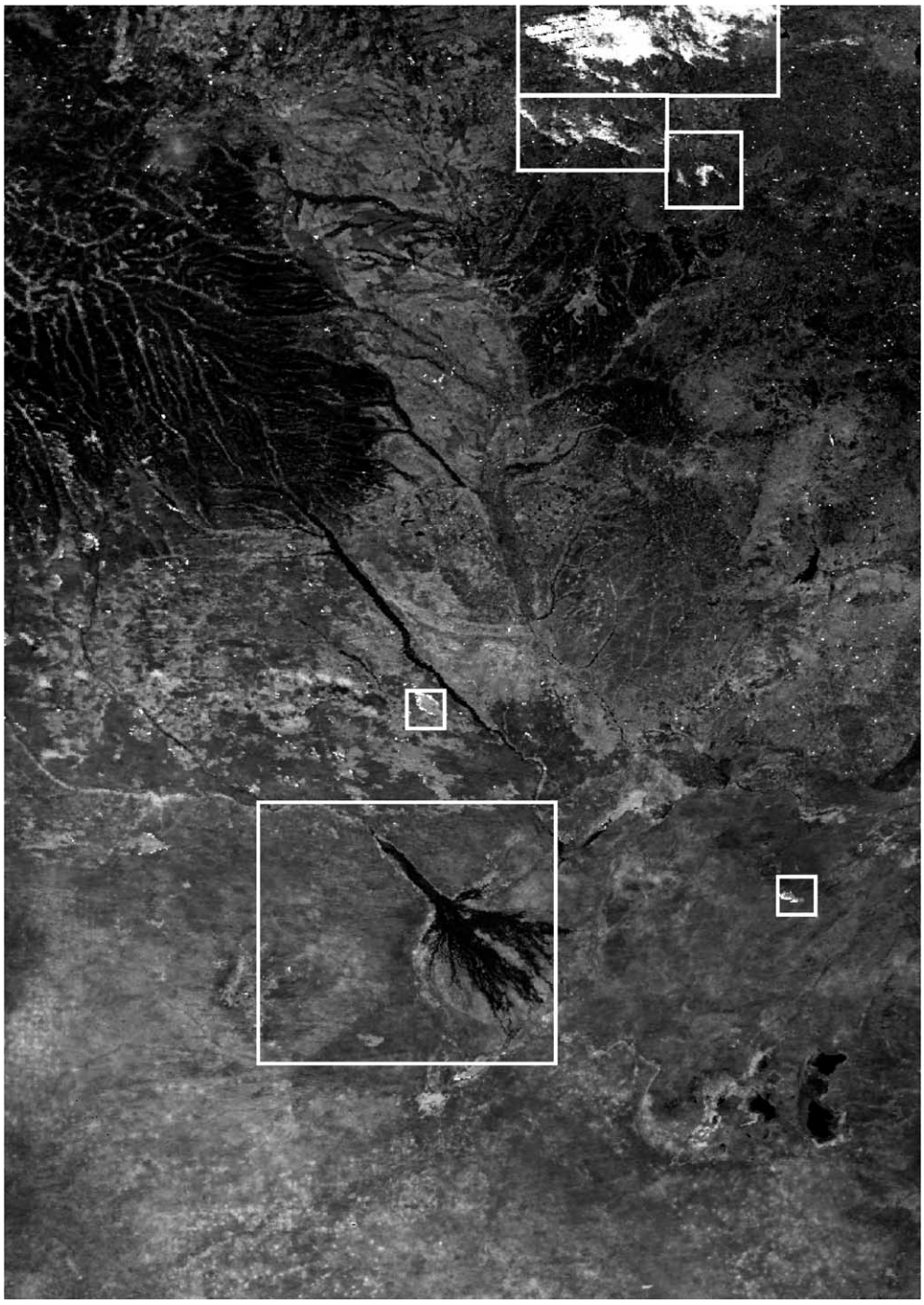

Fig. 15. Gray scale image of the surface reflectance computed in band 20 (scaled between 0.0 and 0.25 reflectance unit). The brightest feature on the images corresponds to fire (small boxes) and clouds (top boxes). Granule acquisition time is 8:55, August 25th, 2000. Image is in geographic projection centered on 18.63° South and 23.24° East.

thermal infrared (bands 31 and 32) ranges from 0.93 for bare soils up to unity for vegetation covered areas. This general trend—bare soils with low emissivity, vegetation covered areas with emissivity close to unity—agree with laboratory measurements of emissivity spectrum (Salisbury & D'Aria, 1994; Snyder et al., 1997). In general, minerals and rocks have low emissivity all over the infrared spectrum and vegetation has high emissivity. This trend is probably due to the amount of water in organic matter, the water emissivity being very close to unity all over the infrared.

However, the link between the vegetation coverage and thermal emissivity is not so straightforward. Maps of emissivity in MODIS bands shows different patterns, especially over the semi-arid areas. When the fraction of bare soils becomes significant, its spectral signature plays an important role in the overall spectral signature of the area. Bare soils present a large variety of spectral signatures, depending on their mineral composition, as well as grain size and moisture (Takashima & Masuda, 1987).

4.4. Fire detection

Fire detection is an important issue that MODIS remote sensing data could address. Experience gained with pre-cursor sensors to MODIS (mainly AVHRR) has driven some of the design of the instrument to enable more efficient fire detection: MODIS is equipped with several bands in the middle infrared with one band (21) set up with a relatively high saturation temperature (500 K). The detection of fire relies on the simple principle that a "hot" surface (between 600 and 1200 K) within a given pixel will generate an apparent difference in temperature between the middle infrared (4 μm) and the thermal infrared (11–12 μm). This is due to the spectral behavior of the Planck function and the usual temperature of the surface and of the fire (Dozier, 1981). The operational fire detection algorithm on MODIS (Justice et al., 2002) relies on the use of the middle infrared and take advantage of the high saturation band in a contextual fire detection approach which has been extensively tested for AVHRR and adopted by the community. We are proposing here to directly estimate the increase of reflectance due to fire, or the reflectance anomaly, as we will later refer to it. For that purpose, we will use as a starting point the middle infrared reflectance which is already corrected for thermal emissions as estimated from the thermal infrared. Fig. 15 shows a gray scale image of the surface reflectance (Julian day 238, 2000) in band 20 (scaled between 0 and 0.25 unit of reflectance). On this image, the highest reflectances observed correspond to cloud, sparsely vegetated areas and active fires. In order to estimate the reflectance anomaly due to fire, we use the 2.13-μm band (MODIS band 7) to derive an empirical relationship with the reflectance in band 20, for an area-free of clouds and fires. The area selected correspond to the big box in Fig. 15. For those pixels, a high correlation exists between the reflectance in bands 7 and 20 (Fig. 16). Using this empirical relationship, we are able to predict the reflectance in band 20 with an uncertainty of the order of 0.01. We used that relationship to "correct" the surface reflectance computed in band 20. Once this correction is done, only pixels with clouds and active fires show a substantial reflectance anomaly. The cloud pixels are filtered (1) using the cirrus band 26 (1.38 μm) and (2) using band 1 corrected for atmospheric effect (0.67 μm) through the empirical relationship used to derive aerosol over land (band $1 = 0.5 \times$ band 7) (Kaufman et al., 1997). The test on band 26 is simply a threshold on the reflectance (0.03). Pixels that exhibit both a strong positive anomaly in the middle infrared ($\rho_{band20} - a \times \rho_{band7}{}^2 - b \times \rho_{band7} > 0.05$) and in band 1 ($\rho_{band1} - 0.5 \times \rho_{band7} > 0.05$) are classified as cloud. Fig. 17 shows the reflectance anomaly ($\rho_{band20} - a \times \rho_{band7}{}^2 - b \times \rho_{band7}$) after cloud filtering. Fig. 17 shows very bright areas (white, anomaly >0.10 reflectance unit) which corresponds to active fire and areas with lower anomaly (gray, ~ 0.05 reflectance unit) which correspond in general to recently burned areas. Based on this anomaly, we can design a very simple fire detection scheme by setting a threshold on the anomaly to select fire. Fig. 18 shows the active fire map that is generated by applying this approach (fires were flagged where the anomaly >0.10). The fires detected are almost always associated with a high aerosol concentration (hazy aspect of the RGB image) and, in a lot of cases, smoke plumes could be associated with the fire detected and there is no obvious contamination by clouds. The detection technique seems fairly sensitive: a rough

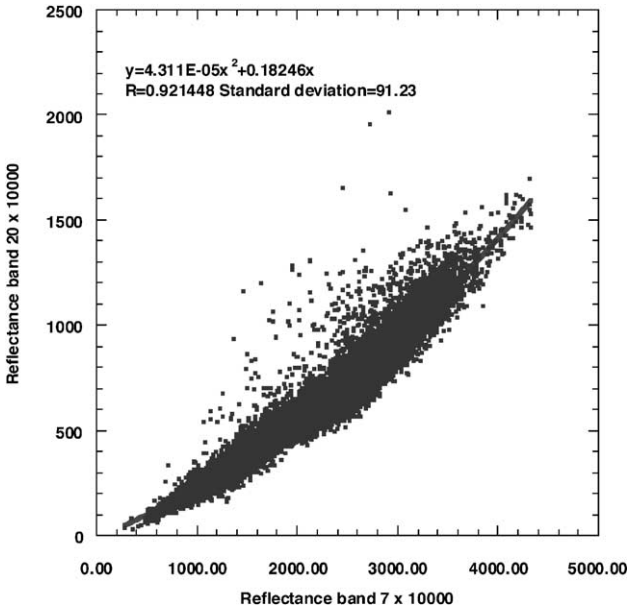

Fig. 16. Empirical relationship derived between the reflectance in band 20 (3.79 μm) and the reflectance in band 7 (2.13 μm) over a cloud free area (big box in Fig. 15).

Fig. 17. Gray scale image of the reflectance anomaly (scaled between 0.0 and 0.25 reflectance unit) observed in band 20 after correcting for surface reflectance estimate based on band 7 (2.13 μm) and filtering clouds.

computation shows that with the threshold used (0.1) and assuming a ''fire'' temperature of 800 K, we will detect fire of about 200 m^2 and above. Some enlarged details of the area inside the blue box are presented in Fig. 18. The aerosol optical depth (bottom left of Fig. 18) shows an important increase from 0.1 (outside the smoke plume) to 1.0 (inside the smoke plume). On the temperature image, several features are noticeable, the highest temperature associated with the burned area (red, orange, yellow) ranging from 312 to 318 K, then the decrease in temperature of 3–4 K in the area covered by the smoke plume (303–304 K) as compared to the background (306–308 K). Since the decrease of the temperature in the smoke plume area is not completely correlated with the optical depth and the size of the smoke plume particles being too small to influence the apparent temperature in the longwave, the effect we are seeing is due to the radiative forcing of the smoke plume which decreases the available incoming radiation in the visible-near-infrared

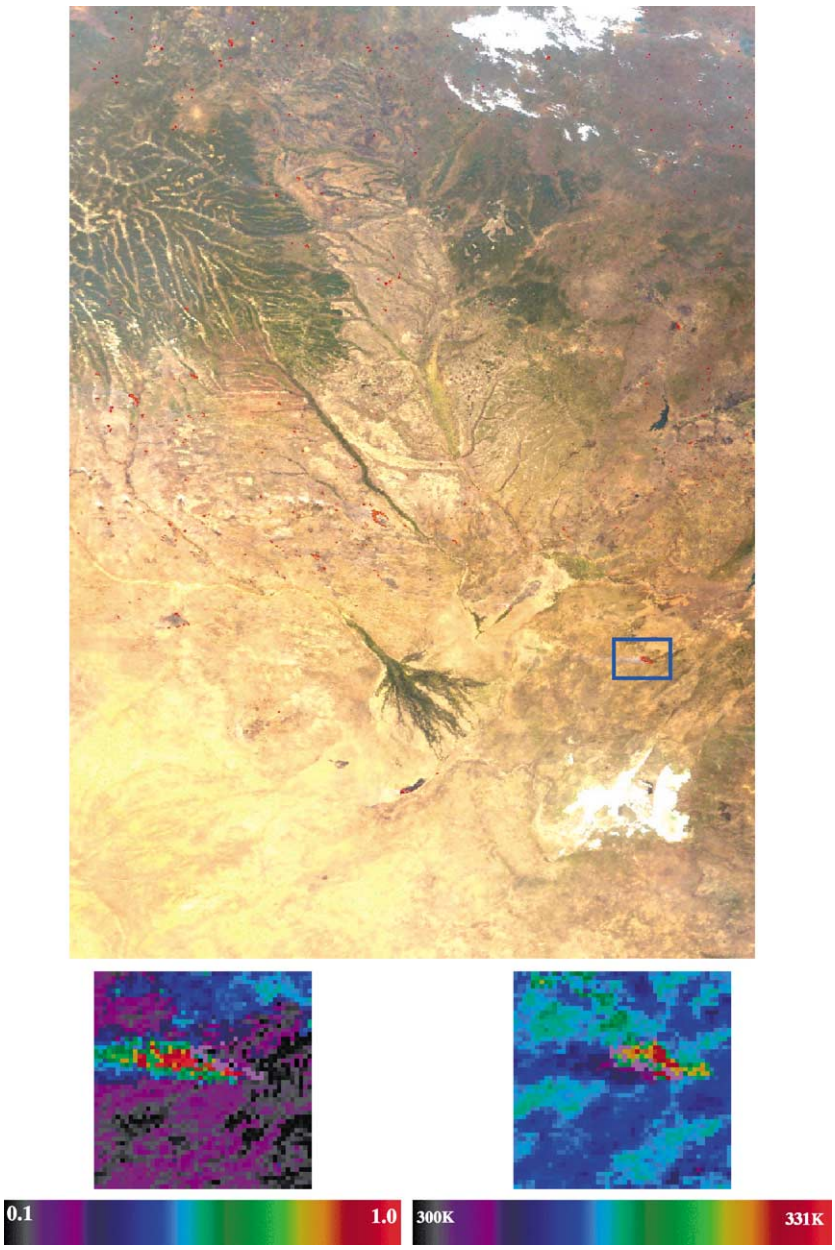

Fig. 18. Active fire map, determined from reflectance anomaly approach. The fire corresponds to the red dot, the background is the surface reflectance product (RGB) not corrected for aerosol. Details of one of the fire (blue box) are presented at the bottom: optical thickness at 470 nm retrieved by MODIS on the left side and surface temperature on the right side.

region, resulting in a cooling of the surface compared to the smoke-free area (Robock, 1988).

Fig. 19 illustrates some preliminary evaluation of the present fire detection algorithm. The comparison was conducted for fires observed over South Africa by both MODIS and Landsat7/ETM+ on August, 31, 2000, located 31.5° East, 23.53° South. The present results are compared to the ETM+ data RGB composite (Red = 1.6 μm, Green = 0.87 μm, Blue = 0.67 μm). On Landsat/ETM+ RGB, the fires appear as red as they are saturating the reflectance at 1.6 μm in the 30×30 m ETM+ pixels. Smoke is visible at 0.67 μm and therefore appears blue. The MODIS detection results are plotted as crosses of different color corresponding to different levels of reflectance anomaly. The white, red, yellow, green and blue crosses correspond, respectively, to anomaly greater than 0.5, 0.4, 0.3, 0.2 and 0.1. The top and bottom of the image shows, both on MODIS and ETM+, a large number of strong fires (white crosses). However, the MODIS detection places the position of the fires further down (South) than the ETM+ data (see polygon A and A′). We explain that difference by the time difference between MODIS (08:20 GMT) and ETM+ (07:40 GMT) acquisitions. In 40 min, the fire front could easily move

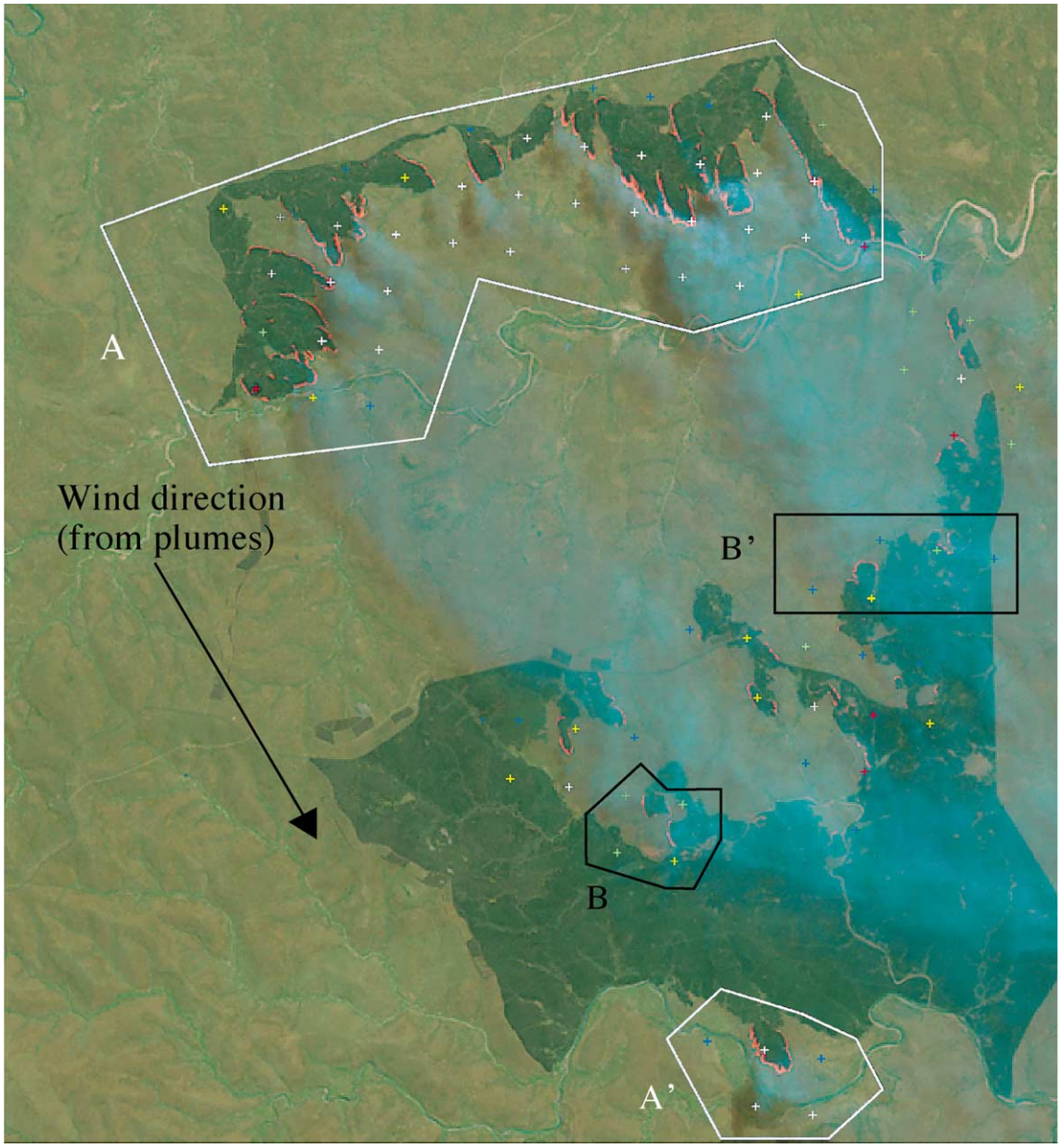

Fig. 19. RGB composition of Landsat/ETM+ data (Red = 1.6 μm, Green = 0.87 μm, Blue = 0.67 μm) with the overlay of the present MODIS fire detection algorithm results (crosses). The white, red, yellow green and blue crosses correspond respectively to anomaly greater than 0.5, 0.4, 0.3, 0.2 and 0.1.

by a couple of kilometers, the direction of the move is coherent with the wind direction that could be inferred from the smoke plumes. Two other areas (B and B′) are interesting, in that there is a real correlation between MODIS and ETM+ data. When examined closely, one can see in both areas that the fire front is progressing against the plumes direction, therefore limiting the progression of fire, which explains the little difference seen between the 40-min apart observations. Overall, this comparison shows a real potential in this approach. We will need to further evaluate this algorithm with ASTER data (coincident with MODIS), to confirm these good performances.

5. Conclusion

Using atmospheric corrections, surface radiances in MODIS bands 20, 22, 23, 29, 31 and 32 are computed, allowing for the retrieval of emissivity ratios (TISIE) with night-time images and middle infrared surface reflectance with day-time images. A BRDF model is fed by the latter, leading to directional emissivity at 3.79, 3.97 and 4.06 μm. Then, using again the emissivity ratios, directional emissivity is obtained at 8.53, 11.02 and 12.03 μm. The accuracy of reflectances is evaluated over water and is of the order of 0.015. By checking the consistency of surface temperature derived at different wavelengths, we assessed the accuracy

of the emissivities to be of the order of 1% and the accuracy of land surface temperature to be of the order of 1 K.

With middle infrared surface reflectance, separation between land surface temperature and emissivity is achieved. The access to the spectral signature in middle and thermal infrared at the scale of MODIS observation is new. In terms of land surface characterization, possibly new information is available from infrared spectral signatures. Surface parameters such as soil moisture might be retrieved by analysis of infrared spectral signatures.

In terms of radiative budget, the output longwave radiation could be derived from infrared spectral signature and land surface temperature, as compared to the Stephen–Boltzmann's law usually adopted. The shortwave radiative budget might also be refined by the availability of middle infrared reflectance. Regarding the atmospheric corrections, NCEP data could be refined with atmospheric data provided by MODIS, whenever the relevant products will be validated.

Middle infrared surface reflectance exhibits another promising application in fire detection. Further validation with coinciding ASTER data will be conducted. Analysis of reflectance anomaly will be investigated and could lead to fire size and temperature determination. These applications of the middle infrared surface reflectance are strong rationales for including bands 20–23 in the MODIS surface reflectance product (MOD09).

References

Acharya, P. K., Anderson, G. P., Berk, A., Chetwynd, J. H., Bernstein, L. S., Kneizys, F. X., Matthew, M. W., Shettle, E. P., Adler-Gloden, S. M., Abreu, L. W., Robertson, D. C., Gallery, W. O., Selby, J. E., & Clough, S. A. (1998). Modtran user's manual versions 3.7 and 4.0, *Technical report*, Air Force Research Laboratory, Space Vehicle Directorate, Air Force Materiel Command, Hanscom AFB, MA 01731-3010 USA.

Becker, F. (1987). The impact of spectral emissivity on the measurement of land surface temperature from a satellite. *International Journal of Remote Sensing*, *10*, 1509–1522.

Becker, F., & Li, Z. L. (1990). Temperature Independent Spectral Indices in thermal infrared bands. *Remote Sensing of Environment*, *32*, 17–33.

Berk, A., Berstein, L. S., & Robertson, D. C. (1989). Modtran: a moderate resolution model for lowtran 7, *Technical Report GL-TR-89-0122*, Optical Physics Division, US Air Force Geophysics Laboratory, Hanscom Air Force Base, MA, USA.

Brown, O. B., Minnett, P. J., Evans, E., Kearns, E., Kilpatrick, K., Kumar, R., & Závody, A. (1999). MODIS sea surface temperature algorithm: Algorithm theoretical basis document, version 2.0, MODIS documentation.

Cox, C., & Munk, W. (1954). Measurement of the roughness of sea surface from photographs of the Sun's glitter. *Journal of Optical Society of America*, *44*(11), 838–850.

Dozier, J. (1981). A method for satellite identification of surface temperature fields of subpixel resolution. *Remote Sensing of Environment*, *11*, 221–229.

Goïta, K., & Royer, A. (1997). Surface temperature and emissivity separability over land surface from combined TIR and SWIR AVHRR data. *IEEE Transactions on Geoscience and Remote Sensing*, *35*(3), 718–733.

Hale, G. M., & Querry, M. R. (1973). Optical constants of water in the 200-nm to 200-μm wavelength region. *Applied Optics*, *12*, 555–563.

Halthore, R. N., Eck, T. F., Holben, B. N., & Markham, B. L. (1997). Sun photometric measurements of atmospheric water vapor column abundance in the 940-nm band. *Journal of Geophysical Research*, *102*(D4), 4343–4352.

Holben, B. N., Eck, T. F., Slutsker, I., Tanre, D., Buis, J. P., Setzer, A., Vermote, E., Reagan, J. A., Kaufman, Y., Nakajima, T., Lavenu, F., Jankowiak, I., & Smirnov, A. (1998). AERONET—a federated instrument network and data archive for aerosol characterization. *Remote Sensing of Environment*, *66*, 1–16.

Justice, C. O., Giglio, L., Korontzi, S., Roy, D., Owens, J., Alleaume, S., Petitcolin, F., Morisette, J., Descloitres, J., & Kaufman, K. (2002). The MODIS fire products: algorithm, preliminary validation, and application. *Remote Sensing of Environment* (this issue).

Kaufman, Y. J., Tanre, D., Remer, L. A., Vermote, E. F., Chu, A., & Holben, B. N. (1997). Operational remote sensing of tropospheric aerosol over land from EOS–MODIS. *Journal of Geophysical Research*, *102*(D14), 17051–17068.

Li, Z. L., Becker, F., Stoll, M. P., & Wan, Z. (1999). Evaluation of six methods for extracting relative emissivity spectra from thermal infrared images. *Remote Sensing of Environment*, *69*, 197–214.

Lucht, W., Schaaf, C. B., & Strahler, A. H. (2000). An algorithm for the retrieval of albedo from space using semiempirical BRDF model. *IEEE Transactions on Geoscience and Remote Sensing*, *38*, 977–998.

Masuda, K., Takashima, Y., & Takayama, Y. (1988). Emissivity of pure and sea waters for the model sea surface in the infrared window regions. *Remote Sensing of Environment*, *24*, 313–329.

Nerry, F., Petitcolin, F., & Stoll, M. P. (1998). Bidirectional reflectivity in AVHRR channel 3: application to a region in northern Africa. *Remote Sensing of Environment*, *66*, 298–316.

Nicodemus, F. E. (1965). Directional reflectance and emissivity of an opaque surface. *Applied Optics*, *4*(7), 767–773.

Petitcolin, F., Nerry, F., & Stoll, M. P. (2002a). Mapping directional emissivity at 3.7 μm using a simple model of bidirectional reflectivity. *International Journal of Remote Sensing* (in press).

Petitcolin, F., Nerry, F., & Stoll, M. P. (2002b). Mapping Temperature Independant Spectral Iindice of Emissivity and directional emissivity in AVHRR channels 4 and 5. *International Journal of Remote Sensing* (in press).

Quin, Z., & Karnieli, A. (1999). Progress in the remote sensing of land surface temperature and ground emissivity using NOAA-AVHRR. *International Journal of Remote Sensing*, *20*(12), 2367–2393.

Robock, A. (1988). Enhancement of surface cooling due to forest fire smoke. *Science*, *242*, 911–913.

Roger, J. C., & Vermote, E. (1998). A method to retrieve the reflectivity signature at 3.75 μm from AVHRR data. *Remote Sensing of Environment*, *64*, 103–114.

Salisbury, J. W., & D'Aria, D. M. (1994). Emissivity of terrestrial materials in the 3–5 μm atmospheric window. *Remote Sensing of Environment*, *47*, 345–361.

Salisbury, J. W., Wald, A., & D'Aria, D. M. (1994). Thermal-infrared remote sensing and Kirchhoff's law 1. Laboratory measurements. *Journal of Geophysical Research*, *99*(B6), 11897–11911.

Snyder, W. C., Wan, Z., Zhang, Y., & Feng, Y. (1997). Thermal infrared (3–14 μm) bidirectional reflectance measurements of sand and soils. *Remote Sensing of Environment*, *60*, 101–109.

Snyder, W. C., Wan, Z., Zhang, Y., & Feng, Y.-Z. (1998). Classification-based emissivity for land surface temperature measurement from space. *International Journal of Remote Sensing*, *19*(14), 2753–2774.

Strahler, A. H., Muller, J. -P., Lucht, W., Schaaf, C. B., Tsang, T., Gao, F., Li, X., Lewis, P., & Barnsley, M.J. (1999). MODIS BRDF/Albedo product: Algorithm theoretical basis document, version 5.0, MODIS documentation.

Takashima, Y., & Masuda, K. (1987). Emissivities of quartz and Sahara dustpowers in the infrared region (7–17 μm). *Remote Sensing of Environment*, *23*, 51–63.

Vermote, E., Tanré, D., Deuzé, J. L., Hermann, M., & Morcrette, J. J. (1997). Second Simulation of the Satellite Signal in the Solar Spectrum, 6S: an overview. *IEEE Transactions on Geoscience and Remote Sensing*, *35*(3), 675–686.

Wan, Z., & Li, Z.-L. (1997). A physics-based algorithm for retrieving land surface emissivity and temperature from EOS/MODIS data. *IEEE Transactions on Geoscience and Remote Sensing*, *35*(4), 980–996.

Wanner, W., Li, X., & Strahler, A. H. (1995). On the derivation of kernel-driven models of bidirectional reflectance. *Journal of Geophysical Research*, *100*(D10), 21077–21089.